

# Experimental and Theoretical Approach of Evaluating Chitosan Ferulic Acid Amide As An Effective Corrosion Inhibitor

Hepziba Magie Jessima S.J (✉ [hepziba.magie@christuniversity.in](mailto:hepziba.magie@christuniversity.in))

Christ University

**S. Subhashini**

Avinashilingam Institute of Home Science and Higher Education for Women: Avinashilingam University for Women

**Avni Berisha**

Universiteti i Prishtinës: Universiteti i Prishtines Hasan Prishtina

**Valbonë Mehmeti**

Universiteti i Prishtinës: Universiteti i Prishtines Hasan Prishtina

**Subramanian Sathy Srikandan**

PSG College of Technology

---

## Research Article

**Keywords:** a. Modified chitosan, b. mild steel, c. corrosion inhibitors, d. EIS, and e. Monte Carlo and molecular dynamic simulation

**Posted Date:** February 11th, 2021

**DOI:** <https://doi.org/10.21203/rs.3.rs-161633/v1>

**License:**   This work is licensed under a Creative Commons Attribution 4.0 International License.

[Read Full License](#)

---

1 **Experimental and theoretical approach of evaluating chitosan ferulic acid amide as an effective corrosion**  
2 **inhibitor**

3 **S.J. Hepziba Magie Jessima<sup>a, b\*</sup> S.Subhashini<sup>b</sup> Avni Berisha<sup>c, d</sup> Valbonë Mehmeti<sup>c</sup> and Subramanian**  
4 **Sathy Srikandan<sup>d</sup>**

5 <sup>a</sup>Department of Chemistry, CHRIST (Deemed to be University), Bengaluru-560029, India

6 <sup>b</sup>Department of Chemistry, Avinashilingam Institute for Home Science and Higher Education for Women  
7 (Deemed to be University), Coimbatore-641043, India

8 <sup>c</sup>Chemistry Department of Natural Sciences Faculty, University of Prishtina, rr. “NënaTereze” nr.5, 10000,  
9 Prishtina, Kosovo

10 <sup>d</sup> Materials Science - Nanochemistry Research Group, NanoAlb – Unit of Albanian Nanoscience and  
11 Nanotechnology, Tirana, Albania.

12 <sup>e</sup>Department of Applied Science, PSG COLLEGE OF TECHNOLOGY, Peelamedu, Coimbatore-641004  
13

14 **Abstract**

15 Phenolic acid grafted chitosan has widespread drug delivery applications, as bio adsorbent, packing  
16 material, etc., due to its excellent antioxidant and antimicrobial properties. However, for the first time, the  
17 anticorrosive efficiency of ferulic acid modified chitosan has been investigated. The prepared chitosan derivative  
18 is characterized using spectral methods, thermal analytical methods, surface charge, and particle size analysis.  
19 The evaluation of corrosion inhibition potential showed a highest value of 95.96 % at 303 K. Thermodynamic  
20 activation and adsorption parameters endorse a mixed adsorption process involving an initial electrostatic  
21 interaction followed by chemisorption. Electrochemical studies gave results which agreed well with the  
22 gravimetric studies. Surface morphological studies were performed using contact angle measurements, FESEM,  
23 EDAX, AFM, optical profilometric and UV spectral techniques. Computational studies involving quantum  
24 chemical calculations, Monte Carlo and molecular dynamic simulation studies, and radial distribution function  
25 analysis are further done to validate the experimental results.

26 **Keywords:** a. Modified chitosan, b. mild steel, c. corrosion inhibitors, d. EIS, and e. Monte Carlo and molecular  
27 dynamic simulation

28  
29  
30 -----  
31 \*Corresponding author. E-mail address: hepziba.magie@christuniversity.in  
32  
33  
34  
35  
36  
37

38 **Highlights**

- 39       ✚ Chitosan ferulic acid amide was evaluated for corrosion inhibition performance
- 40       ✚ I.E of the modified chitosan was found to be 95.96 % for mild steel in 1 M HCl
- 41       ✚ Adsorption process obeyed Langmuir isotherm further supported by  $K_L$  factor
- 42       ✚ Good correlation of experimental results from weight loss and electrochemical studies
- 43       ✚ Experimental results validated by theoretical studies

44

45

46

47

48

49

50

51

52

53

54

55

56

57

58

59

60

61

62

63

64

65

66

67 **Graphical Abstract**

68

69

70

71

72

73

74

75

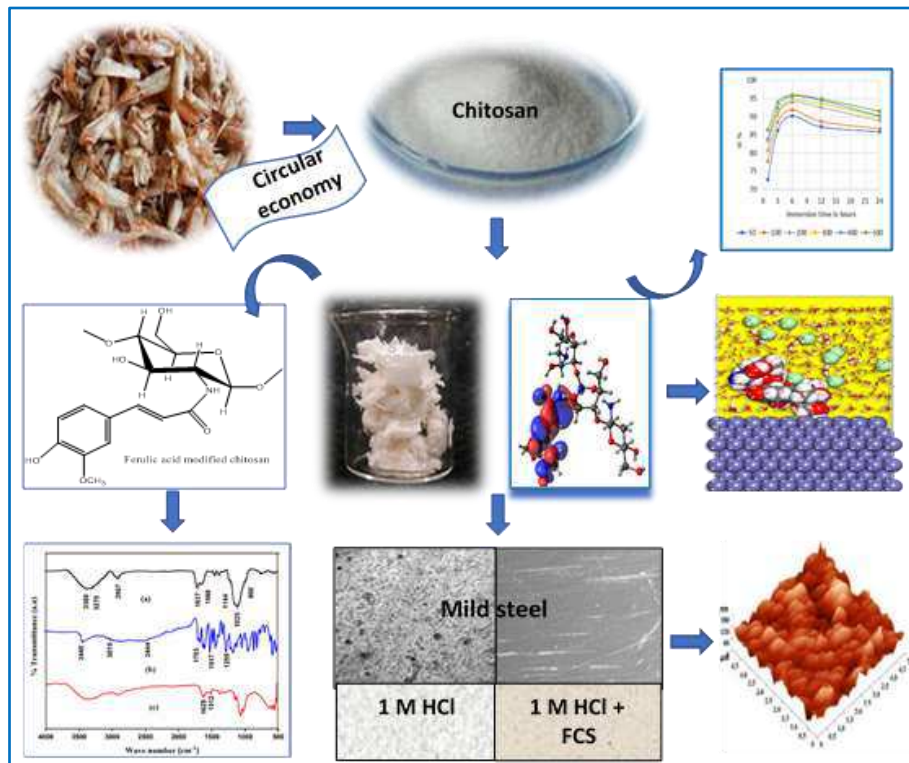
76

77

78

79

80



81

82

83

84

85

86

87

88

89

90

91

92

93

94

## 95 1. INTRODUCTION

96 The acid treatment of metals, namely acid pickling, descaling, etching, etc., renders the metal surface  
97 free from stain, scale, rust, and other impurities. However, this action exposes the clean, bare metal more to the  
98 aggressive medium resulting in an increased metal dissolution. Therefore, corrosion inhibitors are used as  
99 additives in the cleaning acids. These additives mitigate corrosion by adsorbing themselves on the metal surface,  
100 forming a protective film that prevents the metal surface from being exposed to the aggressive environment (Sherif  
101 2014). The use of inhibitors is economical and compatible compared to other mitigation techniques. Besides, it  
102 allows the use of low-grade carbon steel in the place of high-cost alloys (Finšgar and Jackson 2014). There are  
103 numerous corrosion inhibitors tested and proven, but only a few are employed in practice. This observation reveals  
104 that in addition to protection, certain other factors such as cost-effectiveness, eco-friendly, non-toxic nature, ready  
105 availability, and compatibility in combating corrosion also matters. Polymers can act as effective corrosion  
106 inhibitors due to their inherent stability, ability to form complexes that can blanket the metal surface, and multiple  
107 binding sites that help in slower desorption.

108 Many of the natural polymers such as natural gums (Peter et al. 2015; Mobin et al. 2017), pectin (Fares  
109 et al. 2012b; Fiori-Bimbi et al. 2015; Umoren et al. 2015), derivatives of cellulose (Solomon et al. 2010; Li et al.  
110 2015; Sangeetha et al. 2016; Umoren et al. 2018), starch (Zulhusni et al. 2015; Charitha and Rao 2017; Parveen  
111 et al. 2018), carrageen (Khairou et al. 2007; Fares et al. 2012a), alginates (Obot et al. 2017; Jmiai et al. 2018), and  
112 chitosan (Waanders et al. 2002; El-Haddad 2013; Umoren et al. 2013; Gupta et al. 2018; Brou et al. 2020) are  
113 evaluated as potential corrosion inhibitors for different metals in acidic and neutral solutions. However, some  
114 polymers show low solubility in aqueous solutions and undergo decomposition at higher temperatures (Solomon  
115 et al. 2017). Modification of the biopolymers was found to improve the solubility and increase the adsorption sites  
116 in the polymer. The literature survey also reveals the various attempts to relate the antioxidant properties with that  
117 of the anticorrosive behavior in different plant extracts and organic compounds. This survey was done to analyze  
118 whether antioxidative properties can serve as a predictive index to evaluate the corrosion inhibition efficiency (V  
119 V Sher and Voevoda; Boujakhrou et al. 2015; Hussin et al. 2015; Júnior et al. 2016; Momin et al. 2016;  
120 Prabakaran et al. 2019; Vorobyova et al. 2019). Therefore, the present investigation targets the preparation of a  
121 water-soluble corrosion inhibitor with excellent antioxidant properties. By employing chitosan from the seafood  
122 waste, the dire need of the hour, namely practicing circular economy, has been realized in this research work.

123 Chitosan has poly hydroxyl and amine groups that make it an efficient functional material exploited in  
124 various applications (Kumar 2000). Studies on chitosan and its derivatives reveal its efficacy as potential green  
125 corrosion inhibitors. Polyaniline chitosan demonstrated a corrosion inhibition efficiency of 84.78 % for Q<sub>235</sub> mild  
126 steel in the acid medium (Kong et al. 2019). PEG crosslinked chitosan showed an excellent corrosion inhibition  
127 efficiency of 93.9 % for mild steel in sulphamic acid (Chauhan et al. 2018b). Amylose acetate blended  
128 carboxymethyl chitosan records an anticorrosive potential of 97.65 % against mild steel in the acid medium (Erna  
129 et al. 2019). Chitosan-based thiosemicarbazide, thiocarbohydrazide, and Schiff bases also proved to be efficient  
130 green corrosion inhibitors (Menaka and Subhashini 2016; Chauhan et al. 2018a). Chitosan derivatives are proved  
131 to be excellent corrosion mitigators of other metals also (Mohamed and Fekry 2011; Giuliani et al. 2018)

132 In the present investigation, ferulic acid modified chitosan (FCS) was prepared using the method reported  
133 earlier (Woranuch and Yoksan 2013) with slight modification and was characterized using different techniques.  
134 FCS plays a significant role in several biomedical applications, and for the first time, its application in the field

135 of corrosion is explored in the present study. The corrosion mitigation efficiency of FCS was assessed using the  
136 gravimetric method and electrochemical studies. Surface studies serve as evidence for the mitigation potential of  
137 the inhibitor (Jessima et al. 2020a). Theoretical studies were done to validate the experimental results.

138

## 139 **2. EXPERIMENTAL**

### 140 **2.1 Instrumentation**

141 The functional group characterization of FCS was done using ATR-FTIR (Shimadzu IRSpirit), UV-  
142 visible (Shimadzu UV-1800), and proton NMR (Bruker 400 MHz NMR) spectral studies. Thermogravimetric and  
143 differential scanning calorimetric curves were recorded (STA-6000 from Perkin Elmer) to analyze the temperature  
144 response. Malvern Zeta sizer (ZEN 3600) was employed to study the particle charge and size analysis.

145 Gamry Reference - 600 instrument was employed for the electrochemical studies and Echemanalyst  
146 software for interpreting the experimental results

147 Surface morphology studies of the metal samples were done to relate the decrease in metal dissolution  
148 with the inhibitor film formation. The contact angle analyzer, Phoenix 300 Plus model, was used for the contact  
149 angle measurement. Carl Zeiss Sigma V Field Emission Scanning Electron Microscope was employed for SEM  
150 and EDAX analyses. Atomic force microscope (NTDMT model) and optical profilometer (ZETA-20 model),  
151 engaged for surface topography and roughness studies. Images in the optical profilometer captured using a 20x  
152 magnification lens. Zeta 3D software is used for the analysis of the images.

### 153 **2.2 Chemicals and reagents**

154 Chitosan (75 % deacetylated) and ferulic acid (minimum assay of 99.0%) were procured from Hi-Media  
155 Laboratories Pvt. Ltd. The carbodiimide coupling reagent (EDC) and doubly distilled water were procured from  
156 Sisco Research Laboratories Pvt. Ltd. Analar grade concentrated hydrochloric acid, acetone, ethanol, methanol  
157 were used for the investigation. Chitosan was further washed with boiling water, followed by methanol, and dried  
158 in a vacuum desiccator (Giuliani et al. 2018).

### 159 **2.3 Mild steel metal samples**

160 Mild steel samples were cut into strips of 5 x 1 x 0.2 cm dimension and 1 x 1 cm dimension for weight  
161 loss and electrochemical studies. The metal samples were polished with a buff wheel, abraded with fine emery  
162 sheets, cleaned, and degreased before storing in the desiccator for further use.

### 163 **2.4 Preparation of corrosion inhibitor**

164 Chitosan in 25 ml of 0.25 M hydrochloric acid was stirred overnight at room temperature. An equal  
165 amount of ferulic acid is added to the EDC coupling reagent in 10 ml of absolute ethanol. The mixture is then  
166 slowly transferred to the chitosan solution placed on a magnetic stirrer maintained at 60 °C. The stirring was  
167 continued for 3 hours, and the white precipitate obtained was washed with acetone, then kept in a desiccator for  
168 drying. Scheme I display the chemical reaction involved in the preparation of the modified chitosan.

169

#### Scheme I Preparation of FCS

### 170 **2.5 Assessment of anticorrosive performance of FCS**

#### 171 **2.5.1 Gravimetric studies**

172 Prewieghed metal samples in triplicates were held in suitable glass hooks and immersed in 100 ml  
173 beakers containing 0 to 500 ppm concentration of FCS inhibitor in 1 M HCl (Jessima et al. 2020b). The immersion

174 periods chosen for the present study include ½, 1, 3, 6, 12, and 24 hours at 303 K. After the stipulated immersion  
 175 periods, the samples were removed, washed thoroughly with water, and placed in the desiccator. The metal  
 176 samples are weighed again to note the weight loss. The same procedure was repeated for the temperature studies  
 177 done at 303, 313, 323, 333, and 343 K for an immersion period of half an hour. Both the immersion and  
 178 temperature studies were performed in triplicates under aerated and unstirred conditions.

179 The inhibition efficiency ( $\eta_{CI}$ ) of FCS against corrosion was calculated using eq. 1 and corrosion rate  
 180 ( $K_{CR}$ ) using eq. 2.

181 
$$\eta_{CI} = \frac{w_b - w_i}{w_b} \times 100 \text{ -----eq.1}$$

182 
$$K_{CR} \text{ (mpy)} = \frac{3.45 \times 10^6 \times \text{weight loss}}{DAT} \text{ ----- eq.2}$$

183 where  $w_b$  and  $w_i$  represent the weight loss of the metal samples when exposed to 1 M hydrochloric acid and FCS  
 184 solution, respectively.  $D$  is the metal density in  $\text{g/cm}^3$ ,  $A$  is the area of the metal samples in  $\text{cm}^2$  and  $T$  indicates  
 185 the exposure period in hours.

186 **2.5.2 DC and AC electrochemical measurements**

187 Tafel, linear polarization resistance, and AC impedance studies were carried out at room temperature  
 188 under aerated and unstirred conditions using Gamry Reference 600 instrument. Mild steel sample was employed  
 189 as the working electrode, stable and robust saturated calomel electrode as reference electrode, and platinum  
 190 electrode as an auxiliary to complete the cell circuit. The electrochemical impedance spectroscopic studies were  
 191 performed at a frequency range of 100 kHz to 0.01 Hz with 10 mV amplitude as AC signal at steady state open  
 192 circuit potential. Echemanalyst software interpreted the experimental results. Tafel polarization curves were  
 193 obtained by applying a sweeping potential of + 250 mV anodically and -250 mV cathodically versus the open  
 194 circuit potential at 0.1666 mV/sec scan rate. The linear polarization resistance measurements were made at  $\pm 20$   
 195 mV vs. OCP and 0.5 mV/sec scan rate (Jafar Mazumder 2019; Kartsonakis et al. 2020).

196 The percentage of inhibition efficiency of the FCS inhibitor is calculated using  $i_{corr}$  values from Tafel  
 197 studies, LPR values from linear polarisation studies, and  $R_p$  values from impedance studies employing the  
 198 following equations

199 
$$IE_T (\%) = \left( \frac{I_{corr_0} - I_{corr_{inh}}}{I_{corr_0}} \right) \times 100 \text{ ----- eq.3}$$

200 
$$IE_{LPR} (\%) = \left( \frac{LPR_{inh} - LPR_0}{Rp_{inh}} \right) \times 100 \text{ -----eq.4}$$

201 
$$IE_{Rp} (\%) = \left( \frac{Rp_{inh} - Rp_0}{Rp_{inh}} \right) \times 100 \text{ ----- eq.5}$$

202 where  $I_{corr_0}$  and  $I_{corr_{inh}}$ ,  $LPR_0$  and  $LPR_{inh}$ ,  $Rp_0$  and  $Rp_{inh}$  represent the corrosion current density, linear  
 203 polarisation resistance, and polarization resistance obtained when the electrolyte solution was 1 M HCl and  
 204 FCS, respectively

205 **2.6 Theoretical studies**

206 **2.6.1 Quantum chemical calculations**

207 Quantum chemical calculations were done using density functional theory employing Gaussian 09  
 208 software in the framework of the B3LYP/6-31+G (d, p) basis set. Theoretical parameters were calculated for the  
 209 optimized molecular geometry of neutral and protonated FCS. The Mulliken charges generated aided to locate the  
 210 site of protonation, which has the highest negative charge. According to Koopman's theorem, the following  
 211 parameters are related to the energy of the frontier orbitals  $E_{HOMO}$  and  $E_{LUMO}$  by eq.6 and 7.

212 Ionization potential (I) = - E<sub>HOMO</sub>-----eq. 6

213 Electron Affinity (A) = - E<sub>LUMO</sub>-----eq.7

214 According to Mulliken, the electronegativity ( $\chi$ ) is the average value of ionization potential and electron affinity

215 
$$\chi = \frac{I+A}{2} \text{-----eq.8}$$

216 Similarly, the global hardness ( $\eta$ ) is calculated using the eq. 9.

217 
$$\eta = \frac{I-A}{2} \text{-----eq.9}$$

218  $\eta$  is related to the energy gap between the frontier molecular orbitals. The lesser the energy gap, the more is the  
219 softness, and the greater is its chemical reactivity.

220 According to Parr et al., the electrophilicity index ( $\omega$ ) is the natural tendency of a species to accept electrons. The  
221 electrophilicity index ( $\omega$ ) can be calculated using the eq.10

222 
$$\omega = \frac{\chi^2}{4\eta} \text{-----eq.10}$$

223 The quantum parameter  $\Delta N$  is used to evaluate the altitude of the transferred electrons and represented by the  
224 following equation

225 
$$\Delta N = \frac{\phi_{Fe} - \chi_{inh}}{2(\eta_{Fe} + \eta_{inh})} \text{-----eq.11}$$

226 where  $\phi_{Fe}$  refers to the electronegativity of Fe, and its theoretical value is 4.82 eV for (110) plane chosen because  
227 of the higher stabilization energy. The value of  $\eta_{Fe}$  is equal to zero (Dagdag et al. 2019a).

## 228 **2.6.2 Monte Carlo and Molecular Dynamic simulation details**

229 The evaluation of the interaction between the Fe (110) surface and the inhibitor molecule (FCS)  
230 throughout Monte Carlo (MC) and Molecular dynamic (MD) simulation is performed in the simulated corrosion  
231 medium by the use of a seven atom-thick layer unit cell of Fe (110) surface. The slab size used in these calculations  
232 was: 24.842 Å x 24.842 Å x 12.533 Å with a 25 Å vacuum layer. This box is filled with 550 water molecules/1  
233 inhibitor molecule (in neutral or protonated state) / 10 hydronium + 10 chloride ions (Faydy et al. 2020).

234 MD was attained using the NVT at 298 K over a simulation time of 300 ps (using a 1 fs time step and  
235 0.5 ns simulation time) (Hsissou et al. 2019b, 2020b, a; Dagdag et al. 2020d, a). The temperature control is attained  
236 via the Berendsen thermostat (Dagdag et al. 2020e). The recurrently COMPASSII forcefield used in corrosion  
237 studies was used for the MC (Monte Carlo) and MD (Molecular Dynamic) (Sun et al. 2016; Berisha 2019; Dagdag  
238 et al. 2020b; About et al. 2020). The Radial Distribution Function (RDF) analysis is implemented on the complete  
239 trajectory of the MD [38,52].

## 240 **3. RESULTS AND DISCUSSION**

### 241 **3.1 Spectral characterization, thermal stability, and zeta potential analysis of FCS**

242 Comparative infrared spectra of (a) chitosan biopolymer, (b) ferulic acid, and (c) FCS is displayed in Fig  
243 1. The chitosan spectrum shows absorption bands at 3270 -368 cm<sup>-1</sup> arising due to N-H and O-H stretching  
244 vibrations. This band also includes intramolecular hydrogen bond characteristic of polysaccharides. The  
245 symmetric and asymmetric stretching of C-H bonds occur at 2911 and 2867 cm<sup>-1</sup>. The C=O and C-N stretching  
246 vibrations of the N-acetyl group are found at 1637 cm<sup>-1</sup> and 1317 cm<sup>-1</sup>. The absorbance band found at 1568 cm<sup>-1</sup>  
247 is due to N-H bending vibrations of the primary amine. CH<sub>2</sub> bending vibrations and CH<sub>3</sub> symmetrical deformations  
248 are identified at 1420 cm<sup>-1</sup> and 1381 cm<sup>-1</sup>, respectively. IR peaks at 1144 cm<sup>-1</sup>, 1059 cm<sup>-1</sup> and 1025 cm<sup>-1</sup> corresponds

249 to the C-O-C bridge and C-O asymmetric stretching. The C-H bending vibrations of out of plane of the  
250 monosaccharide ring correspond to the peak at  $900\text{ cm}^{-1}$  (Queiroz et al. 2015). Ferulic acid has the following  
251 characteristic peaks, namely O-H stretching at  $3448\text{ cm}^{-1}$  and C-H stretching at  $2911\text{-}3015\text{ cm}^{-1}$ , C=O stretching  
252 of the carboxyl group at  $1703\text{ cm}^{-1}$ , C=C of the aromatic ring at  $1517\text{ cm}^{-1}$ , and C-O stretching of the carboxylic  
253 group at  $1272\text{ cm}^{-1}$  (Almeida et al. 2018). The new peak at  $1512\text{ cm}^{-1}$  corresponds to C=C of the aromatic ring  
254 that serves as evidence for FCS formation. The intensity of C=O and N-H stretching bands of the amide group  
255 found at  $1625\text{ cm}^{-1}$  and  $1553\text{ cm}^{-1}$  is also increased. The increased peak intensity at  $2926\text{ cm}^{-1}$  can be attributed  
256 to C-H stretching. The disappearance of the N-H absorption peak of the primary amine at  $1589\text{ cm}^{-1}$  further  
257 supports the grafting process (Woranuch and Yoksan 2013; Li and Li 2017). There is no IR peak at  $1730\text{ cm}^{-1}$   
258 that confirms the absence of ester formation.

259 **Fig 1** Comparative IR spectrum of (a) Chitosan biopolymer (b) Ferulic acid and (c) FCS

260

261 Fig 2 displays the UV visible spectra of chitosan biopolymer, ferulic acid, and FCS. Chitosan in 1%  
262 acetic acid is found to give no absorption peak in the entire spectral range from 250 nm to 400 nm. An ethanolic  
263 solution of ferulic acid shows an absorbance maximum at 290 nm and 321 nm. FCS in 1 M HCl solution shows  
264 the same absorbance maxima at 321 nm that supports chitosan ferulic acid amide (Woranuch and Yoksan 2013;  
265 Chatterjee et al. 2016). Some literature studies also have highlighted redshift for ferulic acid grafted chitosan (Liu  
266 et al. 2017)

267 **Fig 2** Comparative UV spectrum of (a) Chitosan, (b) Ferulic acid, and (c) FCS

268 The chemical structure of the FCS inhibitor is further characterized using  $^1\text{H}$  NMR spectra portrayed in  
269 Fig 3. The  $\text{D}_2\text{O}$  solvent peak is found at 4.8 ppm, and the proton signals at 3.8 ppm, 6.3 ppm, and 7.6 ppm  
270 correspond to  $-\text{OCH}_3$  and methine protons  $\text{CH}_{(g)}$ ,  $\text{CH}_{(h)}$  of ferulic acid, respectively. The remaining aromatic  
271 protons, namely  $\text{H}_{(e-f)}$ , show doublet signals at 7.1 ppm, 6.8 ppm, and 7.2 ppm. The proton signals at 5.2 ppm,  
272 3.18 ppm, 3.7- 4.5 ppm correspond to chitosan protons  $\text{H}_{(1-6)}$  (Woranuch and Yoksan 2013).

273 **Fig 3** NMR spectrum of FCS inhibitor

274 Comparative TGA and DSC curves of chitosan and FCS are shown in Fig.S1 (a) and (b), respectively.  
275 TGA curve of chitosan reflects a weight loss of 50% at the degradation temperature range of  $295\text{-}370^\circ\text{C}$ , whereas  
276 that of the modified polymer is  $209\text{-}302^\circ\text{C}$ . The thermal stability of FCS is reduced compared to chitosan  
277 biopolymer. The decrease may be accounted due to the loose packing structure or reduction in the intermolecular  
278 hydrogen bonding (Liu et al. 2014; Li and Li 2017). DSC curve of chitosan shows a broad endothermic peak at  
279  $122^\circ\text{C}$  that corresponds to the loss of moisture content bound to the polymeric backbone. The exothermic peak at  
280  $337^\circ\text{C}$  is attributed to the decomposition of chitosan. In contrast, the endothermic and exothermic peaks of FCS  
281 are found at lower temperatures than chitosan, i.e., at  $114^\circ\text{C}$  and  $210^\circ\text{C}$ , respectively (Woranuch and Yoksan  
282 2013).

283 Fig S2 (a) and (b) reveals the zeta potential value and the average particle diameter distribution of FCS are  
284  $+49.5\text{ mV}$  and  $383.3\text{ nm}$ , respectively. Polymers with a zeta potential value greater than  $30\text{ mV}$  can show a more  
285 stable dispersion as the particles repel each other (Rahman et al. 2018)(Elbasuney et al. 2019). Corrosion inhibitors  
286 with a positive zeta potential value can enhance corrosion protection. The positive surface charge on the inhibitor  
287 thus serves in adhering to the oxidized metal surface through the anions of the acid solution (Huffer et al).

288 **3.2 Measurement of the anticorrosive performance of FCS**

289 **3.2.1 Gravimetric studies**

290 Fig.4 (a) portrays the change in the inhibition efficiency of FCS with varying immersion periods at 303  
291 K. FCS showed the highest value of 95.96 % when the metal samples were immersed in 500 ppm concentration  
292 of inhibitor solution. Such good anticorrosion performance can be corroborated with enhanced adsorption of the  
293 heteroatoms of the inhibitor on the metal surface (Rugmini Ammal et al. 2018). Fig 4 (b) displays the variation in  
294 the corrosion inhibition efficiency of FCS with the change in temperature from 303 to 343 K. The inhibition  
295 potential increases with temperature up to 313 K and after that is found to decrease slowly. Prolonged exposure  
296 of the metal surface to the inhibitor solution (> 6 hours) and an increase in temperature (> 313 K) showed a slight  
297 decrease in the inhibition performance of FCS. The decreased stability of the adsorbed inhibitor on the longer  
298 exposure time and increased metal surface kinetic energy at higher temperatures may have led to the desorption  
299 process and hence a fall in efficiency (Fares et al. 2012b; Fathima et al. 2017).

300 **Fig 4** Change in corrosion inhibition performance of FCS for mild steel in 1 M HCl at  
301 various (a) immersion periods (b) temperatures

302 The corrosion rate and the temperature can be related by the Arrhenius and transition state equations  
303 represented by the eq. 12 and eq. 13.

304 
$$\log K_{CR} = \frac{-E_a}{2.303RT} + \log A \text{ ----- eq. 12}$$

305 
$$\log \frac{K_{CR}}{T} = \frac{R}{Nh} \exp \frac{\Delta S^*}{R} \exp \frac{-\Delta H^*}{RT} \text{ ----- eq. 13}$$

306 where  $E_a$  is the apparent activation energy,  $\Delta S^*$  and  $\Delta H^*$  refers to the entropy and enthalpy of activation. Table 1  
307 lists the activation parameters calculated from the linear plots drawn based on eq. 12 and 13, namely  $\log K_{CR}$  vs.  
308  $1/T$  and  $\log (K_{CR}/T)$  vs.  $1/T$ . The  $E_a$  values of the inhibited solutions are found to be less than that of the uninhibited  
309 solution. Such lower or unchanged  $E_a$  values can be corroborated with the chemical interaction between the  
310 metal and the heteroatoms of the FCS molecules (Larabi et al. 2005; Zhang et al. 2019a). The increased inhibition  
311 performance of FCS with the temperature rise implies that chemisorbed passive film formation is higher than the  
312 dissolution rate. The lowering values of the frequency factor  $A$  can be correlated with the decreased corrosion  
313 rate in the presence of FCS (Khadom et al. 2011). The positive values of  $\Delta H^*$  reveals that the metal dissolution  
314 involves an endothermic process. The negative values of  $\Delta S^*$  declare the decrease in the disorderliness that may  
315 be due to the formation of the more orderly activation complex (A.Noor 2007).

316 **Table 1** Activation parameters for mild steel in acid solution without and with FCS

317 The inhibition efficiency relies on the corrosion inhibitor's quickness to diffuse from the solution to the  
318 metal surface. Thereby, it replaces the adsorbed water molecules and effectively binds to the active sites present  
319 on the surface (Singh et al. 2019). The degree of surface coverage  $\theta$  decides the nature and the mode of inhibitor  
320 adsorption (Arukalam et al. 2014). The  $\theta$  values at different temperatures were calculated using eq.14 and were  
321 fitted into various adsorption isotherm models. Based on the linear regression coefficient  $R^2$  values, Langmuir  
322 adsorption isotherm represented by eq. 15 was found to be the best fit.

323 
$$\text{Surface coverage } \theta = \frac{Wb-Wi}{Wb} \text{ -----eq.14}$$

324 
$$\frac{C}{\theta} = \frac{1}{K_{ads}} + C \text{ -----eq.15}$$

325 where C represents the inhibitor concentration, and  $K_{ads}$  refers to the equilibrium constant. Fig 5 displays the  
 326 Langmuir plot, and slope values are found to deviate from unity. The slope deviation reveals that in addition to  
 327  $R^2$  values, another physical characteristic  $K_L$  of the adsorption isotherm is to be considered for the best fit (Eduok  
 328 and Khaled 2015; Singh et al. 2018).  $K_L$  is referred to as the dimensionless separation factor of inhibitor adsorption  
 329 and is related to  $K_{ads}$  by the following equation

330 
$$K_L = 1 / (1 + K_{ads}C) \text{ -----eq.16}$$

331 The average values of  $K_L$  values calculated based on eq. 6 is displayed in Table 2. According to Eduok and  
 332 Khaled, if  $K_L < 1$ , then the adsorption process is considered favorable. If  $K_L > 1$  or  $K_L = 1$  then, the adsorption  
 333 process is unfavorable or deemed to be irreversible (Eduok and Khaled 2015). Based on this literature, it is clear  
 334 that the FCS inhibitor favors the Langmuir adsorption process.

335 . **Fig 5** Langmuir isotherm plot for mild steel in 1 M HCl without and with FCS

336 Table 2 lists the other adsorption parameters calculated for mild steel in 1 M hydrochloric acid without  
 337 and with FCS inhibitor. The standard free energy of adsorption  $\Delta G_{ads}$  is calculated using the following equation:

338 
$$\Delta G_{ads} = -RT \ln(1 * 10^6 K_{ads}) \text{ -----eq.17}$$

339 where R represents the ideal gas constant, T is the temperature in Kelvin, and  $10^6$  is the value of water  
 340 concentration in ppm (Roy et al. 2014). The negative values of  $\Delta G_{ads}$  support the spontaneity of the adsorption  
 341 process. When the values of  $\Delta G_{ads}$  is less than 20 kJ/mole corresponds to physisorption, and greater than 40  
 342 kJ/mole conforms to chemisorption (Xu et al. 2017). The  $\Delta G_{ads}$  values listed in Table 2 lies between 28 to 32 kJ /  
 343 mol. These values can be corroborated with the initial electrostatic interaction between the FCS inhibitor and the  
 344 metal surface, leading to physisorption. The transfer of electron pairs from the heteroatoms to the empty d orbitals  
 345 of  $Fe^{2+}$  ions and retro donation to the unoccupied  $\pi^*$  orbital of the FCS molecule occurs, resulting in the  
 346 chemisorption process (Espinoza-Vázquez et al. 2019). The value of  $K_{ads}$  also reflects the increased binding of the  
 347 inhibitor molecules on the metal surface (Singh et al. 2018).

348 **Table 2** Adsorption parameters for mild steel in 1 M HCl without and with FCS inhibitor at different  
 349 temperatures

350 **3.2.2 Electrochemical measurement techniques**

351 **3.2.2.1 Polarization/ Tafel studies**

352 Tafel studies help to analyze the influence of the inhibitor to mitigate the corrosion process taking place  
 353 at the anode or cathode or both. Fig 6 illustrates the polarization curves obtained for mild steel at room temperature  
 354 in the absence and presence of FCS inhibitor. The Tafel plot depicts the decrease of current density with an  
 355 increase in FCS concentration. The decrease implies that the inhibitor film formed impedes the passage of  
 356 aggressive ions to the metal surface (Eduok and Khaled 2015). Table 3 display the various corrosion parameters  
 357 obtained from the Tafel polarization curves. The  $E_{corr}$  values can be related to the driving force towards the  
 358 corrosion reaction. Higher  $E_{corr}$  values imply a greater energy requirement for the corrosion reaction to take place  
 359 (Subramanian et al. 2015). The positive shift of  $E_{corr}$  values from -443 mV to -189 mV illustrates the corrosion  
 360 inhibition performance of the inhibitor (Al-Amiery et al. 2016). This potential shift is further supported by the  
 361 lowering of the corrosion current  $i_{corr}$  density (Erna et al. 2019). The change in both anodic ( $\beta_a$ ) and cathodic Tafel  
 362 slopes ( $\beta_c$ ) reveals that the inhibitor influences both cathodic and anodic reactions but predominantly anodic (Al-  
 363 amiery et al. 2018) The LPR values increases with the concentration of the FCS polymer as displayed in Table

364 2. This increase indicates a decreased metal dissolution due to the adsorption of the inhibitor molecules on the  
365 metal surface. The inhibition efficiency calculated using  $i_{corr}$  values showed a maximum of 97.4 % for 500 ppm  
366 concentration which matches with those calculated from LPR values.

367 **Fig 6** Tafel plot for mild steel in 1 M HCl with and without FCS

368 **Table 3** Tafel electrochemical parameters for mild steel in 1 M HCl without and with FCS

### 369 3.2.2.2 AC Electrochemical impedance studies

370 EIS technique has emerged out as an excellent tool to study the effectiveness of the corrosion inhibitors,  
371 both qualitatively and quantitatively (Meeusen et al. 2019). Fig 7 (a) & (b) represents the Nyquist and Bode cum  
372 phase angle plots obtained for mild steel in blank and in the presence of FCS. The Nyquist plot clearly shows an  
373 increase in the diameter of the impedance plot with the inhibitor concentration. This increase can be attributed to  
374 the inhibitor film formation by protecting the metal surface from corrosion (Kumar et al. 2016). The inhibition of  
375 corrosion is further supported by the rise in the phase angle with the increase in the inhibitor's concentration, as  
376 shown in the Bode plot (Yildiz 2015). The Bode plot reveals only one time constant, which can be corroborated  
377 with the corrosion inhibition by the charge transfer process and is not changed by the inhibitor's presence (Solmaz  
378 2014). The semi-circle in the Nyquist plot is not perfect due to the metal surface's inhomogeneity, surface  
379 irregularities, impurities, surface active sites collectively referred as frequency dispersion effect (Espinoza-  
380 Vázquez et al. 2019)(Chakravarthy and Mohana 2014). Table 4 lists the equivalent circuit fitted impedance  
381 parameters, and Fig 8 displays the equivalent circuit. The double-layer capacitance  $C_{dl}$  can be calculated from the  
382  $Y_0$  values using the eq.18.

$$383 C_{dl} = (Y_0 * R_{ct}^{1-n})^{1/n} \text{-----eq.18}$$

384 The decreasing  $C_{dl}$  values and increasing charge transfer resistance ( $R_p$ ) values with FCS concentration can be  
385 correlated with the increased thickness of the protective film leading to an increased corrosion inhibition (Xu et  
386 al. 2019).

387 **Fig 7** (a) Nyquist plot (b) Bodes , phase angle plots for mild steel in 1 M HCl without and with FCS inhibitor  
388 at 303 K

389 **Fig 8** Equivalent circuit

390 **Table 4** EIS parameters for mild steel in 1 M HCl without and with FCS

## 391 3.3 Surface characterization

### 392 3.3.1 Contact angle measurements

393 Fig 9 displays the contact angle of (a) plain metal surface, (b) &(c) the metal surfaces exposed to acid  
394 and acid containing FCS, respectively. An angle of 90° or less indicates that the steel surface is hydrophilic and  
395 higher than 90° hydrophobic. The enhanced hydrophobic nature of the inhibitor immersed metal sample reveals  
396 the FCS's adsorption on the metal surface, leading to the protective film formation (Reddy et al. 2016)(Marijan  
397 Babic 2017).

398 **Fig 9** Contact angle of mild steel surfaces (a) plain (b) exposed to acid (c) exposed to acid containing the FCS  
399 inhibitor

### 400 3.3.2 Field emission scanning electron microscopic analysis

401 Fig.10 (a) portrays the scanning electron microscopic images of the metal surface before exposure to the  
402 acid solution. Fig 10 (b) depicts the extensive damage produced when the metal sample is in contact with the

403 aggressive acid medium in the inhibitor's absence. Fig 10 (c) reflects the resistance offered by the FCS inhibitor  
404 against the metal dissolution as the surface is smooth as that of the plain metal.

405 **Fig 10** SEM image of the mild steel surfaces (a) plain (b) exposed to acid (c) exposed to acid containing FCS

### 406 3.3.3 Energy dispersive x-ray analysis

407 EDAX images with % of different element contents of the bare metal surface, surface exposed to  
408 uninhibited and inhibited acid solution are displayed in Fig.11 (a-c). The Cl and O content on the metal surface  
409 exposed to acid can be corroborated with the formation of corrosion products such as chlorides and oxides on the  
410 metal surface. The decrease in the iron, C, and O content indicates an organic film on the metal surface exposed  
411 to the inhibited acid solution (Hamdy and El-Gendy 2013).

412 **Fig 11** EDAX image of surfaces (a) plain metal (b) exposed to 1 M HCl (c) exposed to 1 M HCl containing  
413 FCS

### 414 3.3.4 Optical profilometric studies

415 Fig 12 (a-c) portrays the optical profilometric images of the bare metal surface and surfaces exposed to  
416 uninhibited and inhibited solution. Arithmetic average roughness value (Sa) and the root mean square roughness  
417 value (Sq) for the well-polished plain metal surface were found to be 1.551  $\mu\text{m}$  and 1.977  $\mu\text{m}$ , respectively. The  
418 metal surface exposed to uninhibited acid solution showed an increased roughness value of 3.371  $\mu\text{m}$  (Sa) and  
419 4.456  $\mu\text{m}$  (Sq). However, the metal surface exposed to an acid solution containing an optimum FCS concentration  
420 has shown a decreased surface roughness value of 1.597  $\mu\text{m}$  (Sa) and 2.305  $\mu\text{m}$  (Sq). This decrease may be  
421 corroborated with the reduction in corrosion in the presence of the inhibitor (Sliem et al. 2019).

422 **Fig 12** 3D images of mild steel surfaces (a) Plain metal (b) exposed to acid and (c) exposed to acid containing  
423 FCS

### 424 3.3.5 Atomic force microscopy (AFM)

425 AFM is a useful tool for monitoring the corrosion processes by visualizing the surface morphology of  
426 different materials. Fig.13 (a-c) and Fig. 14 (a-c) represent 2 D and 3 D AFM images of the bare metal surface,  
427 metal surface exposed to uninhibited and inhibited solution, for 6 hours. It is evident from Table 5 that the average  
428 roughness value and root mean square value of the metal sample exposed to acid containing FCS shows a  
429 significant decrease. This result can be corroborated with the film formed by the inhibitor adsorbed on the metal  
430 surface (Shainy et al. 2016).

431 **Fig 13** AFM (2 D) image of surfaces (a) plain metal (b) exposed to 1 M HCl and (c) exposed to 1 M HCl  
432 containing FCS

433 **Fig 14** AFM (3 D) images of surfaces (a) plain metal (b) exposed to 1 M HCl and (c) exposed to 1 M HCl  
434 containing FCS

435 **Table 5** AFM parameters for mild steel surface exposed to acid without and with FCS

### 436 3.3.6 UV spectral analysis

437 Fig 15 depicts the UV-visible spectra of FCS solution before and after the immersion of mild steel  
438 samples. The UV-vis spectrum of FCS solution before immersion of the metal samples show absorption bands at  
439 290 nm and 321nm. These bands correspond to the  $\pi$ -  $\pi^*$  electronic transitions of the aromatic ring and  $n$ - $\pi^*$   
440 transitions by the lone pair of electrons on the nitrogen and carbonyl group, respectively (Abboud et al. 2007). On  
441 the other hand, the UV-vis spectrum of the FCS solution taken after 6 hours of immersion of metal samples shows  
442 an increase in the absorbance bands from 321 nm to 266 nm (blue shift). Besides, the absorbance band at 290 nm

443 is disappeared. The increase and change in the position of the absorbance band can be corroborated with the strong  
444 interactions of the heteroatoms of the FCS inhibitor and the  $\text{Fe}^{2+}$  ions resulting in the complex formation (Abdel-  
445 Gaber et al. 2006; Meng et al. 2017; Aloysius et al. 2018).

446 **Fig 15** UV-visible spectra of FCS solution before and after introducing the mild steel samples

#### 447 **4 Theoretical studies**

##### 448 **4.1 DFT studies**

449 DFT studies serve as a successful tool in predicting the reciprocity between the inhibitor and the metal.  
450 The theory throws light on the chemical reactivity and selectivity of corrosion inhibitors, thereby aid to propose  
451 a suitable mechanism for the corrosion inhibition process. The quantum chemical calculations were performed for  
452 the neutral FCS molecule and also for the protonated form as the study is done in an acid medium. These  
453 calculations will enable identifying the preferred form of the inhibitor that can selectively interact with the metal  
454 surface.

455 Fig.16 displays the optimized geometry, frontier molecular orbitals, electrostatic potential mapping of  
456 the FCS in both forms. The nitrogen atom in the optimized structure of the neutral FCS possesses the highest  
457 Mulliken value (-0.4578) and therefore was chosen as the site for protonation. The electron density distribution  
458 plots of the frontier molecular orbitals, i.e., HOMO and LUMO orbitals, are useful to locate the preferred sites of  
459 adsorption in the inhibitor molecules. The electron distribution is solely on the ferulic acid moiety and the methyl  
460 group of the methoxy group of the ferulic acid moiety is found to contribute to a smaller extent to the HOMO and  
461 no contribution to the LUMO; in both neutral and protonated forms. This suggests the charge transfer by the  $-\text{CH}_3$   
462 group of ferulic acid through s – type HOMO and the heteroatoms of the chitosan moiety to the vacant orbital d  
463 orbital of the Fe on the mild steel surface (Zhang et al. 2019b). The electrostatic potential structure reveals the  
464 nucleophilic region (red color) and the electrophilic region (blue) of the FCS inhibitor (Xu et al. 2018).

465 Table 6 gives quantum chemical parameters calculated based on the density functional theory for the  
466 neutral and protonated FCS molecule. The  $E_{\text{HOMO}}$  and  $E_{\text{LUMO}}$  values provide valuable information regarding the  
467 electron donating and accepting capacity of the neutral and protonated FCS molecule. The greater the value of  
468  $E_{\text{HOMO}}$ , the more it behaves as an electron donor, and the lower  $E_{\text{LUMO}}$  value characterizes electron acceptors.  
469 When an inhibitor shows a tendency to donate electrons to the metal surface and at the same time tends to accept  
470 the electrons back donated by the metal, then stronger is the adsorption process (Fouda et al. 2017; Chauhan et al.  
471 2018b). Table 6 reveals that neutral and protonated molecules behave as an electron donor and a good electron  
472 acceptor, respectively. This behavior can be corroborated with the increased global electronegativity ( $\chi$ ),  
473 electrophilicity index ( $\omega$ ) values of the protonated FCS molecule, and the higher fraction of the electron transfer  
474 ( $\Delta N$ ) value for the neutral molecule (Chauhan et al. 2018b). Electrophilicity index value denotes the energy  
475 stabilization after accepting the additional electrons from the environment. The energy gap ( $\Delta E$ ) between the  
476 frontier molecular orbitals measures the kinetic stability of the corrosion inhibitor (Gece 2015). Smaller energy  
477 gap values indicate lesser kinetic stability and hence greater reactivity with the metal surface. Thus, protonated  
478 form contributes to the better performance of the inhibitor than that of the neutral molecule. Dipole moment ( $\mu$ )  
479 values can be related to the electrostatic interaction between the inhibitor molecules and the metal surface. The  
480 higher values of the dipole moment reveal that protonated molecule contributes physisorption process compared  
481 to that of the neutral molecule (Malekmohammadi Nouri and Attar 2015).

482

483 **Fig 16** Optimized molecular structure, frontier MO and electrostatic potential mapping of neutral and protonated  
484 FCS

485 **Table 6** Quantum chemical parameters of neutral and protonated FCS molecule

#### 486 4.2 Monte Carlo and Molecular Dynamic simulation studies

487 The interaction of the FCS and FCS-H+ onto the Fe (110) surface offers a mean to calculate the  
488 adsorption energetics of this adsorption process. Quantitatively, this is done by calculating the adsorption energy  
489 (E<sub>ads</sub>) using the following equation (Mehmeti and Berisha 2017; Dagdag et al. 2019b, 2020c; Hsissou et al. 2019a,  
490 2020a; El Arrouji et al. 2020; Rbaa et al. 2020b, a; Thaçi et al. 2020; Jessima et al. 2020a):

$$491 E_{adsorption} = E_{Fe(110)||FCS \text{ or } FCS-H+} - (E_{Fe(110)} + E_{FCS \text{ or } FCS-H+}) \text{-----eq.19}$$

492 where  $E_{Fe(110)||FCS \text{ or } FCS-H+}$  is the total energy of the simulated corrosion system,  $E_{Fe}$ , and  $E_{FCS \text{ or } FCS-H+}$   
493 are the total energy values of the Fe(110) surface and the free inhibitor molecules (in their neutral or protonated  
494 state) (Jessima et al. 2020a).

495 The lowest energy configuration of FCS and FCS-H+ on the Fe (110) surface is presented in Fig 17. The  
496 inhibitor is absorbed on the Fe (110) surface in a geometry that takes advantage of the surface contact through its  
497 oxygen atoms.

498 The energy values (in terms of different contributions) over the random MC configuration search are  
499 shown in Fig 18. After 3000000 MC steps as perceived from the graph, the value of total average energy is  
500 equilibrated, indicating that the lowest energy configuration of the inhibitors was attained.

501 The E<sub>ads</sub> distribution of the FCS and FCS-H+ inhibitor gained by a massive number of unsystematic  
502 configurations from Monte Carlo calculations (values of adsorption energies for ten lowest energy poses are  
503 presented in supporting information Table S1) is presented in Fig 19.

504 **Fig 17** MC poses the lowest adsorption configurations for the FCS and FCS-H+ in the simulated corrosion  
505 media on the Fe (1 1 0) surface

506 **Fig 18** The presentation of the different energy terms contributions during the Monte Carlo calculations  
507 for FCS (neutral) and FCS-H+ (protonated) inhibitor molecule

508 **Fig 19** Distribution of adsorption energies for: FCS (neutral) and FCS-H+ (protonated) inhibitor onto  
509 the Fe(110) surface

510 The E<sub>ads</sub> onto Fe surface values (Fig 17) for the FCS adsorption is from -239.35 to -285.55 kcal/mol  
511 (with the maximum value of E<sub>ads</sub> probability distribution at -262.15 kcal/mol). The adsorption energies are higher  
512 for the protonated form of the FCS molecule (namely FCS-H+). They are in the range of -372.95 to -415.86  
513 kcal/mol (with the maximum value of E<sub>ads</sub> probability distribution at -395.85 kcal/mol). These huge E<sub>ads</sub> are  
514 suggestive of a strong adsorptive interaction of this inhibitor with the Fe (110) surface (Hsissou et al. 2019a, c;  
515 Dagdag et al. 2020d)

516 MD poses presented in Fig 20, show that the adsorption of these molecules, although in its neutral state,  
517 only covers a small fraction of the iron surface. In the case of the protonated FCS it's adsorption properties  
518 increase – in this case, the molecule tends to have a flat geometry onto the Fe (1 1 0) surface (the equilibration of  
519 the temperature and the energy terms during the MD simulations are shown in the supporting information).

520 **Fig 20** MD poses the lowest adsorption configurations for the FCS and FCS-H+ in the simulated corrosion  
521 media on the Fe (1 1 0) surface

522 **Fig 21** RDF of heteroatoms (nitrogen and oxygen,) for FCS and FCS-H+ on the Fe surface obtained from MD  
523 trajectory

524 A modest method to attain the information vis-à-vis the adsorption process is to use the RDF peak  
525 appearance distance (Berisha 2020; Dagdag et al. 2020d, e; El Arrouji et al. 2020; Rbaa et al. 2020b). The peak  
526 presence for the FCS and FCS-H+ inhibitor is at a lesser distance than 3.5 Å from the surface of Fe indicates the  
527 chemisorption process, while for physisorption, this is projected at larger distances. As evidenced in Fig 21, the  
528 RDF value for nitrogen and oxygen atoms in the FCS-H+ case is present at 3.01 Å (O) and 3.07 Å (N) from the  
529 Fe (110) surface – an expected value for the chemisorption process. Whereas for the FCS, accountable atoms for  
530 the absorption are oxygen atoms [RDF is 2.97 Å (O)]; the nitrogen atoms, as evidenced from the RDF distance of  
531 8.80 Å (N) are do not contribute to the adsorption process. The corresponding RDF analysis support that the  
532 chemisorption is involved during the adsorption of the inhibitor that decreases the corrosion rate of the Fe (110)  
533 surface (Dagdag et al. 2019b, 2020c; Hsissou et al. 2019c, 2020b, c; About et al. 2020).

#### 534 **Conclusion**

- 535 • The corrosion inhibition performance of FCS reached 95.96 % at 500 ppm and 6 hours of immersion  
536 period.
- 537 • The present investigation reveals a chemical interaction between the Fe<sup>2+</sup> ions on the metal surface and  
538 the heteroatoms of the FCS molecules during the adsorption process.
- 539 • Tafel studies showed that the FCS inhibitor was a mixed type inhibiting both the cathodic hydrogen  
540 evolution and anodic dissolution of the mild steel metal.
- 541 • Protonated molecule contributes to the inhibitor efficiency more than that of the neutral molecule.
- 542 • FCS shows that it is an efficient, green corrosion inhibitor that can be used as an additive during acid  
543 cleaning of mild steel.
- 544 • MC and MD calculations validate that there is a vigorous adsorptive interaction that takes place amongst  
545 the FCS inhibitor (in the neutral and protonated state) and the Fe surface. The obtained theoretical results  
546 are in good agreement with the experimental results.

547

#### 548 **Declarations**

549 The authors declare that they have no known competing financial interests or personal relationships that could  
550 have appeared to influence the work reported in this paper.

551 Declarations of interest: None

552

#### 553 **Compliance with Ethical Standards**

554 **Conflict of Interest:** On behalf of all authors, the corresponding author states that there is no conflict of interest.

555 **Credit author statement**

556 **S J Hepziba Magie Jessima:** Conceptualization, Methodology, Writing- Original draft preparation. **Avni**  
557 **Berisha and Valbonë Mehmeti:** Writing, computational software Monte Carlo simulation studies, **Subramanian**  
558 **Sathy Srikandan:** Electrochemical studies **S. Subhashini:** Supervision., Reviewing and Editing,

559

560 **Acknowledgments**

561 The authors would like to thank Indian Institute of Science, Bangalore, India for doing the computational analysis.  
562 Avni Berisha gratefully acknowledges the support from the Ministry of Education, Science and Technology of  
563 Kosovo (Nr.2-5069) for providing the computing resources.

564

565 **References**

566 A.Noor E (2007) Temperature Effects on the Corrosion Inhibition of Mild Steel in Acidic Solutions by Aqueous  
567 Extract of Fenugreek Leaves. *Int J Electrochem Sci* 2:996–1017

568 Abboud Y, Abourriche A, Saffaj T, et al (2007) 2,3-Quinoxalinedione as a novel corrosion inhibitor for mild  
569 steel in 1 M HCl. *Mater Chem Phys* 105:1–5. <https://doi.org/10.1016/j.matchemphys.2007.03.037>

570 About S, Zouarhi M, Chebabe D, et al (2020) Galactomannan as a new bio-sourced corrosion inhibitor for iron  
571 in acidic media. *Heliyon* 6:. <https://doi.org/10.1016/j.heliyon.2020.e03574>

572 Abdel-Gaber AM, Abd-El-Nabey BA, Sidahmed IM, et al (2006) Inhibitive action of some plant extracts on the  
573 corrosion of steel in acidic media. *Corros Sci* 48:2765–2779. <https://doi.org/10.1016/j.corsci.2005.09.017>

574 Al-Amiery AA, Binti Kassim FA, Kadhum AAH, Mohamad AB (2016) Synthesis and characterization of a  
575 novel eco-friendly corrosion inhibition for mild steel in 1 M hydrochloric acid. *Sci Rep* 6:1–13.  
576 <https://doi.org/10.1038/srep19890>

577 Al-amiery AA, Othman MH, Adnan T, et al (2018) Results in Physics Electrochemical studies of novel  
578 corrosion inhibitor for mild steel in 1 M hydrochloric acid. *Results Phys* 9:978–981.  
579 <https://doi.org/10.1016/j.rinp.2018.04.004>

580 Almeida RR, Silva Damasceno ET, de Carvalho SYB, et al (2018) Chitosan nanogels condensed to ferulic acid  
581 for the essential oil of *Lippia origanoides* Kunth encapsulation. *Carbohydr Polym* 188:268–275.  
582 <https://doi.org/10.1016/j.carbpol.2018.01.103>

583 Aloysius A, Ramanathan R, Christy A, et al (2018) Experimental and theoretical studies on the corrosion  
584 inhibition of vitamins – Thiamine hydrochloride or biotin in corrosion of mild steel in aqueous chloride  
585 environment. *Egypt J Pet* 27:371–381. <https://doi.org/10.1016/j.ejpe.2017.06.003>

586 Arukalam IO, Madu IO, Ijomah NT, et al (2014) Acid Corrosion Inhibition and Adsorption Behaviour of Ethyl  
587 Hydroxyethyl Cellulose on Mild Steel Corrosion. *J Mater* 2014:1–11.  
588 <https://doi.org/10.1155/2014/101709>

589 Berisha A (2019) The influence of the grafted aryl groups on the solvation properties of the graphyne and  
590 graphdiyne- A MD study. *Open Chem* 17:703–710. <https://doi.org/10.1515/chem-2019-0083>

- 591 Berisha A (2020) Experimental, Monte Carlo and Molecular Dynamic Study on Corrosion Inhibition of Mild  
592 Steel by Pyridine Derivatives in Aqueous Perchloric Acid. *Electrochem* 1:188–199.  
593 <https://doi.org/10.3390/electrochem1020013>
- 594 Boujakhrouf A, Hamdani I, Chahboun N, et al (2015) Antioxidant activity and corrosion inhibitive behavior of  
595 *Garcinia cola* seeds on mild steel in hydrochloric medium. *J Mater Environ Sci* 6:3655–3666
- 596 Brou YS, Coulibaly NH, Diki NGYS, et al (2020) Chitosan biopolymer effect on copper corrosion in 3.5 wt.%  
597 NaCl solution: Electrochemical and quantum chemical studies. *Int J Corros Scale Inhib* 9:182–200.  
598 <https://doi.org/10.17675/2305-6894-2020-9-1-11>
- 599 Chakravarthy MP, Mohana KN (2014) Adsorption and corrosion inhibition characteristics of some nicotinamide  
600 derivatives on mild steel in hydrochloric acid solution. *ISRN Corros* 2014:1–13.  
601 <https://doi.org/10.1155/2014/687276>
- 602 Charitha BP, Rao P (2017) Starch as an ecofriendly green inhibitor for corrosion control of 6061-Al alloy. *J*  
603 *Mater Environ Sci* 8:78–89
- 604 Chatterjee NS, Anandan R, Navitha M, et al (2016) Development of thiamine and pyridoxine loaded ferulic  
605 acid-grafted chitosan microspheres for dietary supplementation. *53:551–560*.  
606 <https://doi.org/10.1007/s13197-015-2044-4>
- 607 Chauhan DS, Ansari KR, Sorour AA, et al (2018a) Thiosemicarbazide and thiocarbohydrazide functionalized  
608 chitosan as ecofriendly corrosion inhibitors for carbon steel in hydrochloric acid solution. *Int J Biol*  
609 *Macromol* 107:1747–1757. <https://doi.org/10.1016/j.ijbiomac.2017.10.050>
- 610 Chauhan DS, Srivastava V, Joshi PG, Quraishi MA (2018b) PEG cross-linked Chitosan: a biomacromolecule as  
611 corrosion inhibitor for sugar industry. *Int J Ind Chem* 9:363–377. [https://doi.org/10.1007/s40090-018-](https://doi.org/10.1007/s40090-018-0165-0)  
612 [0165-0](https://doi.org/10.1007/s40090-018-0165-0)
- 613 Dagdag O, Berisha A, Safi Z, et al (2020a) DGEBA-polyaminoamide as effective anti-corrosive material for  
614 15CDV6 steel in NaCl medium: Computational and experimental studies. *J Appl Polym Sci* 137:48402.  
615 <https://doi.org/10.1002/app.48402>
- 616 Dagdag O, Berisha A, Safi Z, et al (2020b) Highly durable macromolecular epoxy resin as anticorrosive coating  
617 material for carbon steel in 3% NaCl: Computational supported experimental studies. *J Appl Polym Sci*.  
618 <https://doi.org/10.1002/app.49003>
- 619 Dagdag O, Berisha A, Safi Z, et al (2020c) DGEBA-polyaminoamide as effective anti-corrosive material for  
620 15CDV6 steel in NaCl medium: Computational and experimental studies. *J Appl Polym Sci* 137:1–10.  
621 <https://doi.org/10.1002/app.48402>
- 622 Dagdag O, El Harfi A, El Gouri M, et al (2019a) Anticorrosive properties of Hexa (3-methoxy propan-1,2-diol)  
623 cyclotri-phosphazene compound for carbon steel in 3% NaCl medium: gravimetric, electrochemical, DFT  
624 and Monte Carlo simulation studies. *Heliyon* 5:. <https://doi.org/10.1016/j.heliyon.2019.e01340>
- 625 Dagdag O, Hsissou R, Berisha A, et al (2019b) Polymeric-Based Epoxy Cured with a Polyaminoamide as an

626 Anticorrosive Coating for Aluminum 2024-T3 Surface: Experimental Studies Supported by  
627 Computational Modeling. *J Bio- Tribo-Corrosion* 5:1–13. <https://doi.org/10.1007/s40735-019-0251-7>

628 Dagdag O, Hsissou R, El Harfi A, et al (2020d) Fabrication of polymer based epoxy resin as effective anti-  
629 corrosive coating for steel: Computational modeling reinforced experimental studies. *Surfaces and*  
630 *Interfaces* 18:. <https://doi.org/10.1016/j.surfin.2020.100454>

631 Dagdag O, Hsissou R, El Harfi A, et al (2020e) Epoxy resins and their zinc composites as novel anti-corrosive  
632 materials for copper in 3% sodium chloride solution: Experimental and computational studies. *J Mol Liq*  
633 315:113757. <https://doi.org/10.1016/j.molliq.2020.113757>

634 Eduok UM, Khaled M (2015) Corrosion inhibition for low-carbon steel in 1 M H<sub>2</sub>SO<sub>4</sub> solution by phenytoin:  
635 evaluation of the inhibition potency of another “anticorrosive drug.” *Res Chem Intermed* 41:6309–6324.  
636 <https://doi.org/10.1007/s11164-014-1741-3>

637 El-Haddad MN (2013) Chitosan as a green inhibitor for copper corrosion in acidic medium. *Int J Biol Macromol*  
638 55:142–149. <https://doi.org/10.1016/j.ijbiomac.2012.12.044>

639 El Arrouji S, Karrouchi K, Berisha A, et al (2020) New pyrazole derivatives as effective corrosion inhibitors on  
640 steel-electrolyte interface in 1 M HCl: Electrochemical, surface morphological (SEM) and computational  
641 analysis. *Colloids Surfaces A Physicochem Eng Asp* 604:. <https://doi.org/10.1016/j.colsurfa.2020.125325>

642 Elbasuney S, Gobara M, Zorinyan M, et al (2019) The significant role of stabilized colloidal ZrO<sub>2</sub> nanoparticles  
643 for corrosion protection of AA2024. *Environ Nanotechnology, Monit Manag* 12:.  
644 <https://doi.org/10.1016/j.enmm.2019.100242>

645 Erna M, Herdini H, Futra D (2019) Corrosion Inhibition Mechanism of Mild Steel by Amylose-  
646 Acetate/Carboxymethyl Chitosan Composites in Acidic Media. *Int J Chem Eng* 2019:.  
647 <https://doi.org/10.1155/2019/8514132>

648 Espinoza-Vázquez A, Rodríguez-Gómez FJ, Martínez-Cruz IK, et al (2019) Adsorption and corrosion inhibition  
649 behaviour of new theophylline-triazole-based derivatives for steel in acidic medium. *R Soc Open Sci* 6:.  
650 <https://doi.org/10.1098/rsos.181738>

651 Fares MM, Maayta AK, Al-Mustafa JA (2012a) Corrosion inhibition of iota-carrageenan natural polymer on  
652 aluminum in presence of zwitterion mediator in HCl media. *Corros Sci* 65:223–230.  
653 <https://doi.org/10.1016/j.corsci.2012.08.018>

654 Fares MM, Maayta AK, Al-Qudah MM (2012b) Pectin as promising green corrosion inhibitor of aluminum in  
655 hydrochloric acid solution. *Corros Sci* 60:112–117. <https://doi.org/10.1016/j.corsci.2012.04.002>

656 Fathima A, Abdul S, Sethumanickam S (2017) Corrosion inhibition , adsorption and thermodynamic properties  
657 of poly ( vinyl alcohol- cysteine ) in molar HCl. *Arab J Chem* 10:S3358–S3366.  
658 <https://doi.org/10.1016/j.arabjc.2014.01.016>

659 Faydy M El, Benhiba F, Berisha A, et al (2020) An experimental-coupled empirical investigation on the  
660 corrosion inhibitory action of 7-alkyl-8-Hydroxyquinolines on C35E steel in HCl electrolyte. *J Mol Liq*

661 317:113973. <https://doi.org/10.1016/j.molliq.2020.113973>

662 Finšgar M, Jackson J (2014) Application of corrosion inhibitors for steels in acidic media for the oil and gas  
663 industry: A review. *Corros Sci* 86:17–41. <https://doi.org/10.1016/j.corsci.2014.04.044>

664 Fiori-Bimbi M V., Alvarez PE, Vaca H, Gervasi CA (2015) Corrosion inhibition of mild steel in HCL solution  
665 by pectin. *Corros Sci* 92:192–199. <https://doi.org/10.1016/j.corsci.2014.12.002>

666 Fouda AS, Ismail MA, Abousalem AS, Elewady GY (2017) Experimental and theoretical studies on corrosion  
667 inhibition of 4-amidinophenyl-2,2'-bifuran and its analogues in acidic media. *RSC Adv* 7:46414–46430.  
668 <https://doi.org/10.1039/c7ra08092a>

669 Gece G (2015) Corrosion inhibition behavior of two quinoline chalcones: Insights from density functional  
670 theory. *Corros Rev* 33:195–202. <https://doi.org/10.1515/corrrev-2015-0028>

671 Giuliani C, Pascucci M, Riccucci C, et al (2018) Chitosan-based coatings for corrosion protection of copper-  
672 based alloys: A promising more sustainable approach for cultural heritage applications. *Prog Org Coatings*  
673 122:138–146. <https://doi.org/10.1016/j.porgcoat.2018.05.002>

674 Gupta NK, Joshi PG, Srivastava V, Quraishi MA (2018) Chitosan: A macromolecule as green corrosion  
675 inhibitor for mild steel in sulfamic acid useful for sugar industry. *Int J Biol Macromol* 106:704–711.  
676 <https://doi.org/10.1016/j.ijbiomac.2017.08.064>

677 Hamdy A, El-Gendy NS (2013) Thermodynamic, adsorption and electrochemical studies for corrosion  
678 inhibition of carbon steel by henna extract in acid medium. *Egypt J Pet* 22:17–25.  
679 <https://doi.org/10.1016/j.ejpe.2012.06.002>

680 Hsissou R, About S, Berisha A, et al (2019a) Experimental, DFT and molecular dynamics simulation on the  
681 inhibition performance of the DGDCBA epoxy polymer against the corrosion of the E24 carbon steel in  
682 1.0 M HCl solution. *J Mol Struct* 1182:340–351. <https://doi.org/10.1016/j.molstruc.2018.12.030>

683 Hsissou R, About S, Seghiri R, et al (2020a) Evaluation of corrosion inhibition performance of phosphorus  
684 polymer for carbon steel in [1 M] HCl: Computational studies (DFT, MC and MD simulations). *J Mater*  
685 *Res Technol*. <https://doi.org/10.1016/j.jmrt.2020.01.002>

686 Hsissou R, Benhiba F, About S, et al (2020b) Trifunctional epoxy polymer as corrosion inhibition material for  
687 carbon steel in 1.0 M HCl: MD simulations, DFT and complexation computations. *Inorg Chem Commun*  
688 115:107858. <https://doi.org/10.1016/j.inoche.2020.107858>

689 Hsissou R, Benzidia B, Rehioui M, et al (2020c) Anticorrosive property of hexafunctional epoxy polymer  
690 HGTMDAE for E24 carbon steel corrosion in 1.0 M HCl: gravimetric, electrochemical, surface  
691 morphology and molecular dynamic simulations. *Polym Bull* 77:3577–3601.  
692 <https://doi.org/10.1007/s00289-019-02934-5>

693 Hsissou R, Dagdag O, About S, et al (2019b) Novel derivative epoxy resin TGETET as a corrosion inhibition  
694 of E24 carbon steel in 1.0 M HCl solution. Experimental and computational (DFT and MD simulations)  
695 methods. *J Mol Liq* 284:182–192. <https://doi.org/10.1016/j.molliq.2019.03.180>

696 Hsissou R, Dagdag O, About S, et al (2019c) Novel derivative epoxy resin TGETET as a corrosion inhibition  
697 of E24 carbon steel in 1.0 M HCl solution. Experimental and computational (DFT and MD simulations)  
698 methods. *J Mol Liq* 284:182–192. <https://doi.org/10.1016/j.molliq.2019.03.180>

699 Huffer et al Anticorrosion pigments with positive zeta potential

700 Hussin MH, Shah AM, Rahim AA, et al (2015) Antioxidant and anticorrosive properties of oil palm frond  
701 lignins extracted with different techniques. *Ann For Sci* 72:17–26. [https://doi.org/10.1007/s13595-014-](https://doi.org/10.1007/s13595-014-0405-1)  
702 0405-1

703 Jafar Mazumder MA (2019) Synthesis, characterization and electrochemical analysis of cysteine modified  
704 polymers for corrosion inhibition of mild steel in aqueous 1 M HCl. *RSC Adv* 9:4277–4294.  
705 <https://doi.org/10.1039/c8ra09833f>

706 Jessima SJHM, Berisha A, Srikanth SS, Subhashini S (2020a) Preparation, characterization, and evaluation of  
707 corrosion inhibition efficiency of sodium lauryl sulfate modified chitosan for mild steel in the acid  
708 pickling process. *J Mol Liq* 114382. <https://doi.org/10.1016/j.molliq.2020.114382>

709 Jessima SJHM, Subhashini S, Arulraj J (2020b) Sunova spirulina Powder as an Effective Environmentally  
710 Friendly Corrosion Inhibitor for Mild Steel in Acid Medium. *J Bio- Tribo-Corrosion* 6:.  
711 <https://doi.org/10.1007/s40735-020-00370-x>

712 Jmiai A, El Ibrahim B, Tara A, et al (2018) Alginate biopolymer as green corrosion inhibitor for copper in 1 M  
713 hydrochloric acid: Experimental and theoretical approaches. *J Mol Struct* 1157:408–417.  
714 <https://doi.org/10.1016/j.molstruc.2017.12.060>

715 Júnior JMF, de Vasconcelos Silva MG, Monteiro JA, et al (2016) Evaluation of antioxidant activity and  
716 inhibition of corrosion by brazilian plant extracts and constituents. *Int J Electrochem Sci* 11:3862–3875.  
717 <https://doi.org/10.20964/110388>

718 Kartsonakis IA, Stamatogianni P, Karaxi EK, Charitidis CA (2020) Comparative study on the corrosion  
719 inhibitive effect of 2-mecaptobenzothiazole and Na<sub>2</sub>HPO<sub>4</sub> on industrial conveying API 5L X42 pipeline  
720 steel. *Appl Sci* 10:.  
<https://doi.org/10.3390/app10010290>

721 Khadom AA, Yaro AS, Studies WL (2011) Protection of Low Carbon Steel in Phosphoric Acid by Potassium  
722 Iodide 1. 47:662–669. <https://doi.org/10.1134/S2070205111050078>

723 Khairou KS, Alfi AA, Mabrouk EM (2007) Natural polymers as corrosion inhibitors for aluminium and tin in  
724 acidic media. *Mater Sci Res India* 4:279–290. <https://doi.org/10.13005/msri/040207>

725 Kong P, Feng H, Chen N, et al (2019) Polyaniline/chitosan as a corrosion inhibitor for mild steel in acidic  
726 medium. *RSC Adv* 9:9211–9217. <https://doi.org/10.1039/c9ra00029a>

727 Kumar MNVR (2000) A review of chitin and chitosan applications. *A Rev chitin chitosan Appl* 46:1–27

728 Kumar S, Vashisht H, Olasunkanmi LO, et al (2016) Experimental and theoretical studies on inhibition of mild  
729 steel corrosion by some synthesized polyurethane tri-block co-polymers. *Sci Rep* 6:1–18.

730 <https://doi.org/10.1038/srep30937>

731 Larabi L, Harek Y, Benali O, Ghalem S (2005) Hydrazone derivatives as corrosion inhibitors for mild steel in 1  
732 M HCl. 54:256–262. <https://doi.org/10.1016/j.porgcoat.2005.06.015>

733 Li C, Li J Bin (2017) Preparation of chitosan-ferulic acid conjugate: Structure characterization and in the  
734 application of pharmaceuticals. *Int J Biol Macromol* 105:1539–1543.  
735 <https://doi.org/10.1016/j.ijbiomac.2017.04.103>

736 Li MM, Xu QJ, Han J, et al (2015) Inhibition action and adsorption behavior of green inhibitor Sodium  
737 carboxymethyl cellulose on copper. *Int J Electrochem Sci* 10:9028–9041

738 Liu J, Pu H, Liu S, et al (2017) Synthesis, characterization, bioactivity and potential application of phenolic acid  
739 grafted chitosan: A review. *Carbohydr Polym*. <https://doi.org/10.1016/j.carbpol.2017.07.014>

740 Liu J, Wen X yuan, Lu J feng, et al (2014) Free radical mediated grafting of chitosan with caffeic and ferulic  
741 acids: Structures and antioxidant activity. *Int J Biol Macromol* 65:97–106.  
742 <https://doi.org/10.1016/j.ijbiomac.2014.01.021>

743 Malekmohammadi Nouri P, Attar MM (2015) Experimental and quantum chemical studies on corrosion  
744 inhibition performance of fluconazole in hydrochloric acid solution. *Bull Mater Sci* 38:499–509.  
745 <https://doi.org/10.1007/s12034-015-0865-4>

746 Marijan Babic (2017) Role of Interfacial Chemistry on Wettability and Carbon Dioxide Corrosion of Mild  
747 Steels

748 Meeusen M, Zardet L, Homborg AM, et al (2019) A complementary electrochemical approach for time-resolved  
749 evaluation of corrosion inhibitor performance. *J Electrochem Soc* 166:C3220–C3232.  
750 <https://doi.org/10.1149/2.0271911jes>

751 Mehmeti V V., Berisha AR (2017) Corrosion study of mild steel in aqueous sulfuric acid solution using 4-  
752 methyl-4h-1,2,4-triazole-3-thiol and 2-mercaptosuccinic acid-an experimental and theoretical study. *Front*  
753 *Chem* AUG:1–12. <https://doi.org/10.3389/fchem.2017.00061>

754 Menaka R, Subhashini S (2016) Chitosan Schiff base as eco-friendly inhibitor for mild steel corrosion in 1 M  
755 HCl. *J Adhes Sci Technol* 30:1622–1640. <https://doi.org/10.1080/01694243.2016.1156382>

756 Meng Y, Ning W, Xu B, et al (2017) Inhibition of mild steel corrosion in hydrochloric acid using two novel  
757 pyridine Schiff base derivatives: A comparative study of experimental and theoretical results. *RSC Adv*  
758 7:43014–43029. <https://doi.org/10.1039/c7ra08170g>

759 Mobin M, Rizvi M, Olasunkanmi LO, Ebenso EE (2017) Biopolymer from Tragacanth Gum as a Green  
760 Corrosion Inhibitor for Carbon Steel in 1 M HCl Solution. *ACS Omega* 2:3997–4008.  
761 <https://doi.org/10.1021/acsomega.7b00436>

762 Mohamed RR, Fekry AM (2011) Antimicrobial and anticorrosive activity of adsorbents based on chitosan  
763 schiff's base. *Int J Electrochem Sci* 6:2488–2508

764 Momin MIK, Bahadur I, Ebenso EE, et al (2016) Antioxidant properties, computational studies and corrosion  
765 inhibition potential of 3-hydroxy-1-(2-hydroxyphenyl)-5-(phenyl)-2,4-pentadien-1-one analogues. *J Mol*  
766 *Liq* 223:819–827. <https://doi.org/10.1016/j.molliq.2016.08.107>

767 Obot IB, Onyechu IB, Kumar AM (2017) Sodium alginate: A promising biopolymer for corrosion protection  
768 of API X60 high strength carbon steel in saline medium. *Carbohydr Polym* 178:200–208.  
769 <https://doi.org/10.1016/j.carbpol.2017.09.049>

770 Parveen M, Mobin M, Zehra S, Aslam R (2018) L-proline mixed with sodium benzoate as sustainable inhibitor  
771 for mild steel corrosion in 1M HCl: An experimental and theoretical approach. *Sci Rep* 8:1–18.  
772 <https://doi.org/10.1038/s41598-018-24143-2>

773 Peter A, Obot IB, Sharma SK (2015) Use of natural gums as green corrosion inhibitors: an overview. *Int J Ind*  
774 *Chem* 6:153–164. <https://doi.org/10.1007/s40090-015-0040-1>

775 Prabakaran M, Hemapriya V, Kim SH, Chung IM (2019) Evaluation of Antioxidant and Anticorrosion  
776 Properties of *Epipremnum aureum*. *Arab J Sci Eng* 44:169–178. [https://doi.org/10.1007/s13369-018-](https://doi.org/10.1007/s13369-018-3398-5)  
777 [3398-5](https://doi.org/10.1007/s13369-018-3398-5)

778 Queiroz MF, Melo KRT, Sabry DA, et al (2015) Does the use of chitosan contribute to oxalate kidney stone  
779 formation? *Mar Drugs* 13:141–158. <https://doi.org/10.3390/md13010141>

780 Rahman MM, Zahir H, Haq B, Shehri DA Al (2018) Corrosion Inhibition Properties of Waterborne poly  
781 urethane/cerium nitrate coatings on mild steel. *Coatings*. <https://doi.org/10.3390/coatings8010034>

782 Rbaa M, Dohare P, Berisha A, et al (2020a) New Epoxy sugar based glucose derivatives as eco friendly  
783 corrosion inhibitors for the carbon steel in 1.0 M HCl: Experimental and theoretical investigations. *J*  
784 *Alloys Compd* 833:154949. <https://doi.org/10.1016/j.jallcom.2020.154949>

785 Rbaa M, Ouakki M, Galai M, et al (2020b) Simple preparation and characterization of novel 8-  
786 Hydroxyquinoline derivatives as effective acid corrosion inhibitor for mild steel: Experimental and  
787 theoretical studies. *Colloids Surfaces A Physicochem Eng Asp* 602:125094.  
788 <https://doi.org/10.1016/j.colsurfa.2020.125094>

789 Reddy CM, Sanketi BD, Narendra Kumar S (2016) Corrosion inhibition of mild steel by *Capsicum annum* fruit  
790 paste. *Perspect Sci* 8:603–605. <https://doi.org/10.1016/j.pisc.2016.06.033>

791 Roy P, Karfa P, Adhikari U, Sukul D (2014) Corrosion inhibition of mild steel in acidic medium by  
792 polyacrylamide grafted Guar gum with various grafting percentage : Effect of intramolecular synergism.  
793 *Corros Sci*. <https://doi.org/10.1016/j.corsci.2014.07.039>

794 Rugmini Ammal P, Prajila M, Joseph A (2018) Effective inhibition of mild steel corrosion in hydrochloric acid  
795 using EBIMOT, a 1, 3, 4-oxadiazole derivative bearing a 2-ethylbenzimidazole moiety: Electro analytical,  
796 computational and kinetic studies. *Egypt J Pet* 27:823–833. <https://doi.org/10.1016/j.ejpe.2017.12.004>

797 Sangeetha Y, Meenakshi S, Sairam Sundaram C (2016) Corrosion inhibition of aminated hydroxyl ethyl  
798 cellulose on mild steel in acidic condition. *Carbohydr Polym* 150:13–20.

799 <https://doi.org/10.1016/j.carbpol.2016.05.002>

800 Shainy KM, Rugmini Ammal P, Unni KN, et al (2016) Surface Interaction and Corrosion Inhibition of Mild  
801 Steel in Hydrochloric Acid Using Pyoverdine, an Eco-Friendly Bio-molecule. *J Bio- Tribo-Corrosion* 2:1–  
802 12. <https://doi.org/10.1007/s40735-016-0050-3>

803 Sherif ESM (2014) *The Role of Corrosion Inhibitors in Protecting Metallic Structures against Corrosion in*  
804 *Harsh Environments*. Elsevier B.V.

805 Singh A, Ansari KR, Quraishi MA, Lgaz H (2018) Effect of electron donating functional groups on corrosion  
806 inhibition of J55 steel in a sweet corrosive environment: Experimental, density functional theory, and  
807 molecular dynamic simulation. *Materials (Basel)* 12:. <https://doi.org/10.3390/ma12010017>

808 Singh A, Ituen EB, Ansari KR, et al (2019) Surface protection of X80 steel using Epimedium extract and its  
809 iodide-modified composites in simulated acid wash solution: A greener approach towards corrosion  
810 inhibition. *New J Chem* 43:8527–8538. <https://doi.org/10.1039/c9nj01691k>

811 Sliem MH, Afifi M, Bahgat Radwan A, et al (2019) AEO7 Surfactant as an Eco-Friendly Corrosion Inhibitor for  
812 Carbon Steel in HCl solution. *Sci Rep* 9:1–16. <https://doi.org/10.1038/s41598-018-37254-7>

813 Solmaz R (2014) Investigation of adsorption and corrosion inhibition of mild steel in hydrochloric acid solution  
814 by 5-(4-Dimethylaminobenzylidene)rhodanine. *Corros Sci* 79:169–176.  
815 <https://doi.org/10.1016/j.corsci.2013.11.001>

816 Solomon MM, Gerengi H, Umoren SA (2017) Carboxymethyl Cellulose/Silver Nanoparticles Composite:  
817 Synthesis, Characterization and Application as a Benign Corrosion Inhibitor for St37 Steel in 15% H<sub>2</sub>SO<sub>4</sub>  
818 Medium. *ACS Appl Mater Interfaces* 9:6376–6389. <https://doi.org/10.1021/acsami.6b14153>

819 Solomon MM, Umoren SA, Udoso II, Udoh AP (2010) Inhibitive and adsorption behaviour of carboxymethyl  
820 cellulose on mild steel corrosion in sulphuric acid solution. *Corros Sci* 52:1317–1325.  
821 <https://doi.org/10.1016/j.corsci.2009.11.041>

822 Subramanian B, Maruthamuthu S, Rajan ST (2015) Biocompatibility evaluation of sputtered zirconium-based  
823 thin film metallic glass-coated steels. *Int J Nanomedicine* 10:17–29. <https://doi.org/10.2147/IJN.S79977>

824 Sun H, Jin Z, Yang C, et al (2016) COMPASS II: extended coverage for polymer and drug-like molecule  
825 databases. *J Mol Model* 22:1–10. <https://doi.org/10.1007/s00894-016-2909-0>

826 Thaçi V, Hoti R, Berisha A, Bogdanov J (2020) Corrosion study of copper in aqueous sulfuric acid solution in  
827 the presence of (2E,5E)-2,5-dibenzylidenecyclopentanone and (2E,5E)-bis[(4-  
828 dimethylamino)benzylidene]cyclopentanone: Experimental and theoretical study. *Open Chem* 18:1412–  
829 1420. <https://doi.org/10.1515/chem-2020-0172>

830 Umoren SA, AlAhmary AA, Gasem ZM, Solomon MM (2018) Evaluation of chitosan and carboxymethyl  
831 cellulose as ecofriendly corrosion inhibitors for steel. *Int J Biol Macromol* 117:1017–1028.  
832 <https://doi.org/10.1016/j.ijbiomac.2018.06.014>

- 833 Umoren SA, Banera MJ, Alonso-Garcia T, et al (2013) Inhibition of mild steel corrosion in HCl solution using  
834 chitosan. *Cellulose* 20:2529–2545. <https://doi.org/10.1007/s10570-013-0021-5>
- 835 Umoren SA, Obot IB, Madhankumar A, Gasem ZM (2015) Performance evaluation of pectin as ecofriendly  
836 corrosion inhibitor for X60 pipeline steel in acid medium: Experimental and theoretical approaches.  
837 *Carbohydr Polym* 124:280–291. <https://doi.org/10.1016/j.carbpol.2015.02.036>
- 838 V V Sher and Voevoda Comparative study of the anti oxidant and anti corrosion properties of metal dialkyl and  
839 diaryldithiophosphates. *Chem Technol Fuels Oils* 5:305–307
- 840 Vorobyova VI, Skiba MI, Shakun AS, Nahirniak S V. (2019) Relationship between the inhibition and  
841 antioxidant properties of the plant and biomass wastes extracts - A Review. *Int J Corros Scale Inhib*  
842 8:150–178. <https://doi.org/10.17675/2305-6894-2019-8-2-1>
- 843 Waanders FB, Vorster SW, Geldenhuys AJ (2002) Biopolymer corrosion inhibition of mild steel:  
844 Electrochemical/Mössbauer results. *Hyperfine Interact* 139–140:133–139.  
845 <https://doi.org/10.1023/A:1021271005989>
- 846 Woranuch S, Yoksan R (2013) Preparation, characterization and antioxidant property of water-soluble ferulic  
847 acid grafted chitosan. *Carbohydr Polym* 96:495–502. <https://doi.org/10.1016/j.carbpol.2013.04.006>
- 848 Xu S, Zhang S, Guo L, et al (2019) Experimental and theoretical studies on the corrosion inhibition of carbon  
849 steel by two indazole derivatives in HCl medium. *Materials (Basel)* 12:1–11.  
850 <https://doi.org/10.3390/ma12081339>
- 851 Xu X, Singh A, Sun Z, et al (2017) Theoretical, thermodynamic and electrochemical analysis of biotin drug as  
852 an impending corrosion inhibitor for mild steel in 15% hydrochloric acid. *R Soc Open Sci* 4:.  
853 <https://doi.org/10.1098/rsos.170933>
- 854 Xu Y, Zhang S, Li W, et al (2018) Experimental and theoretical investigations of some pyrazolo-pyrimidine  
855 derivatives as corrosion inhibitors on copper in sulfuric acid solution. *Appl Surf Sci* 459:612–620.  
856 <https://doi.org/10.1016/j.apsusc.2018.08.037>
- 857 Yildiz R (2015) An electrochemical and theoretical evaluation of 4,6-diamino-2-pyrimidinethiol as a corrosion  
858 inhibitor for mild steel in HCl solutions. *Corros Sci* 90:544–553.  
859 <https://doi.org/10.1016/j.corsci.2014.10.047>
- 860 Zhang HH, Qin CK, Chen Y, Zhang Z (2019a) Inhibition behaviour of mild steel by three new benzaldehyde  
861 thiosemicarbazone derivatives in 0.5 M H<sub>2</sub>SO<sub>4</sub>: experimental and computational study. *R Soc Open*  
862 *Sci* 6:190192. <https://doi.org/10.1098/rsos.190192>
- 863 Zhang W, Li HJ, Wang M, et al (2019b) Highly effective inhibition of mild steel corrosion in HCl solution by  
864 using pyrido[1,2-a]benzimidazoles. *New J Chem* 43:413–426. <https://doi.org/10.1039/C8NJ04028A>
- 865 Zulhusni MDM, Othman NK, Lazim AM (2015) Enhancement of corrosion resistance of carbon steel by  
866 *Dioscorea Hispida* starch in NaCl. *AIP Conf Proc* 1678:.. <https://doi.org/10.1063/1.4931277>

867

868

869

870

# Figures

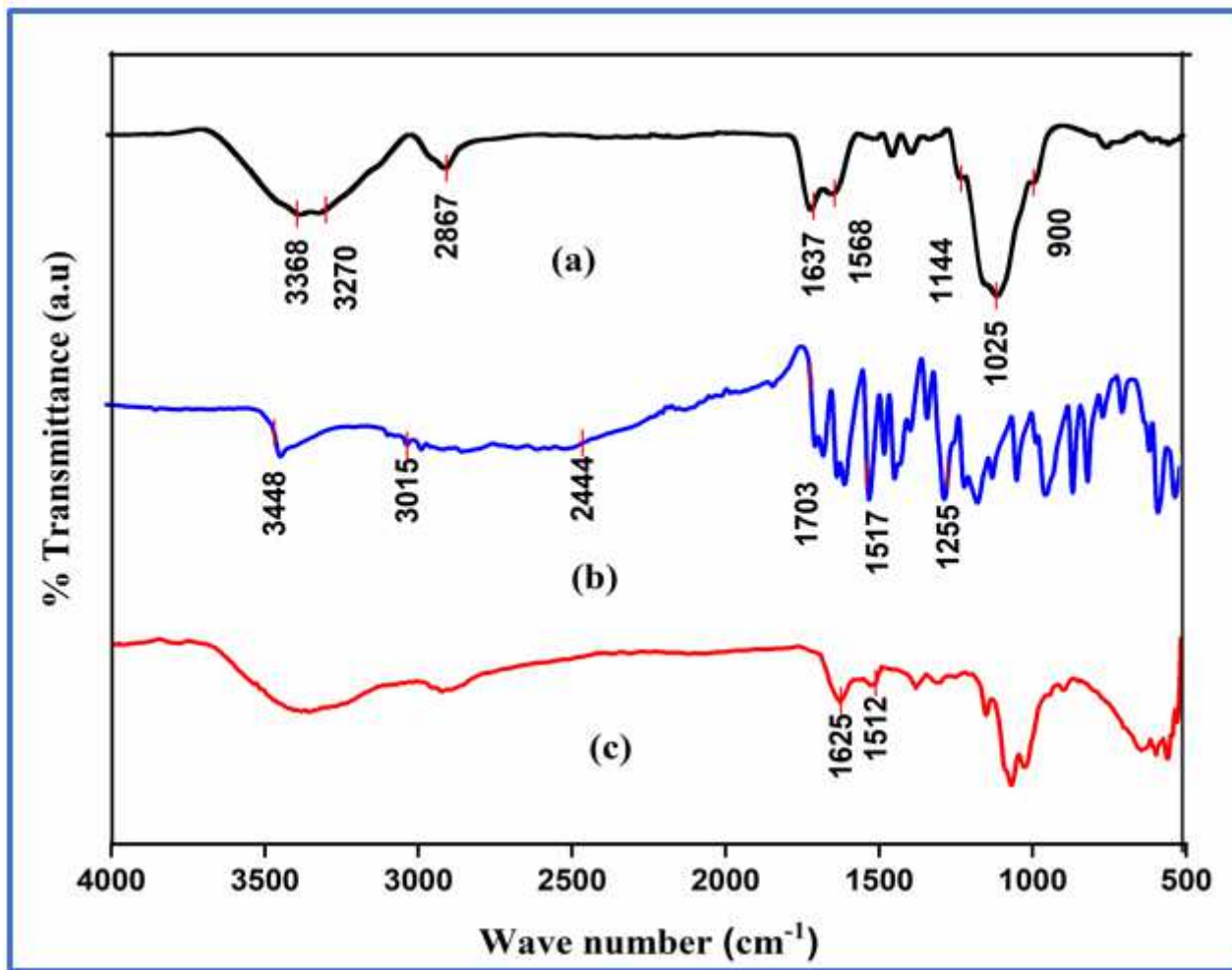


Figure 1

Comparative IR spectrum of (a) Chitosan biopolymer (b) Ferulic acid and (c) FCS

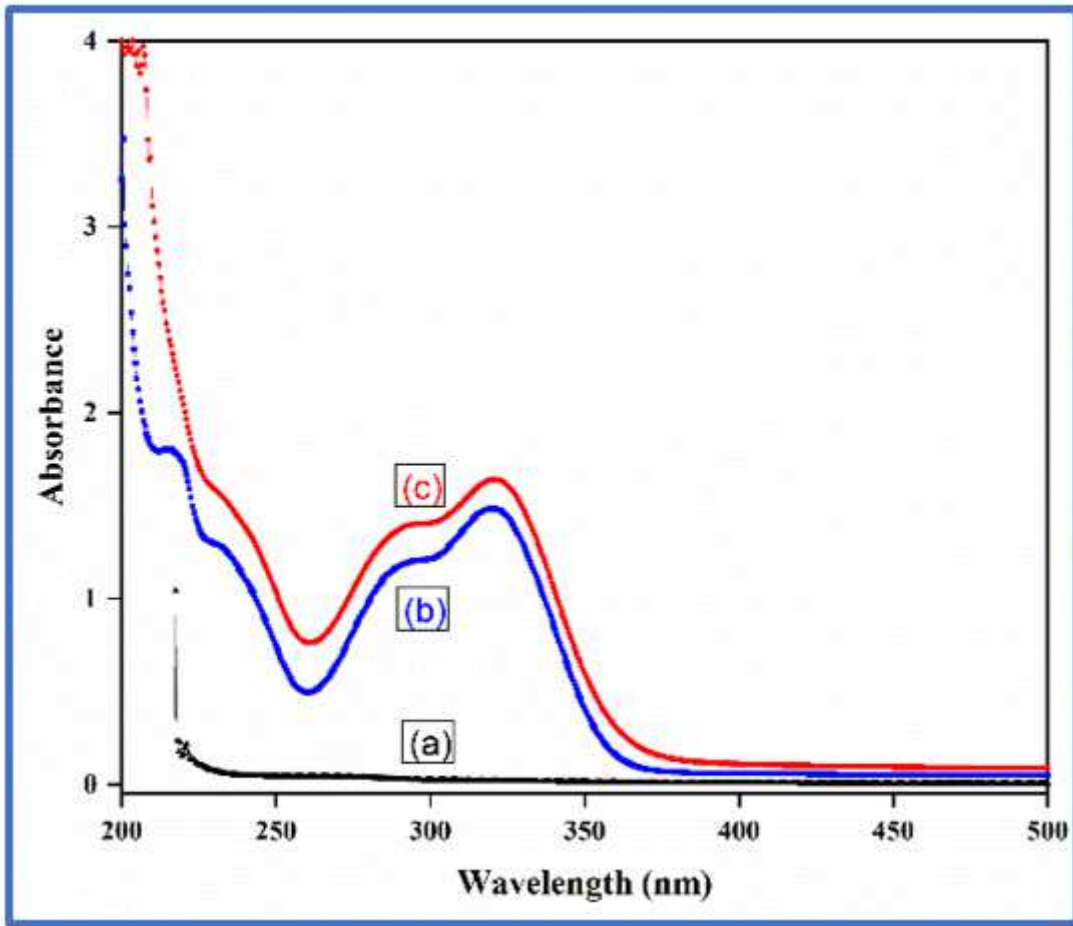


Figure 2

Comparative UV spectrum of (a) Chitosan, (b) Ferulic acid, and (c) FCS

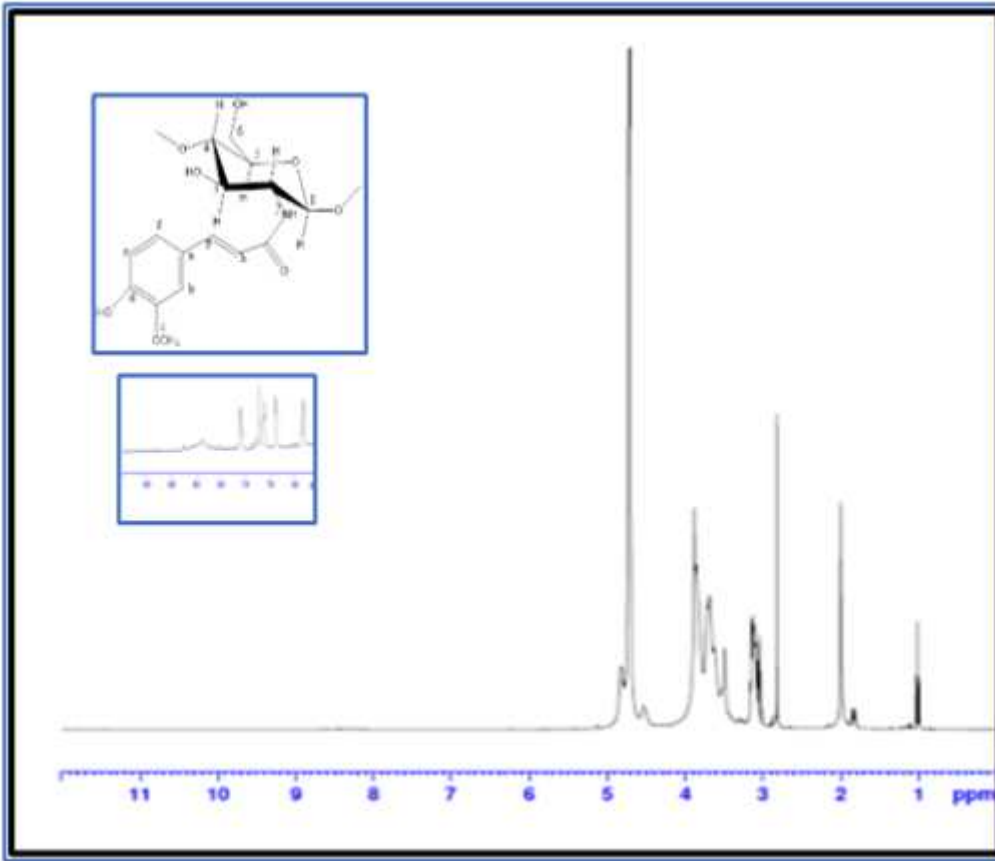


Figure 3

NMR spectrum of FCS inhibitor

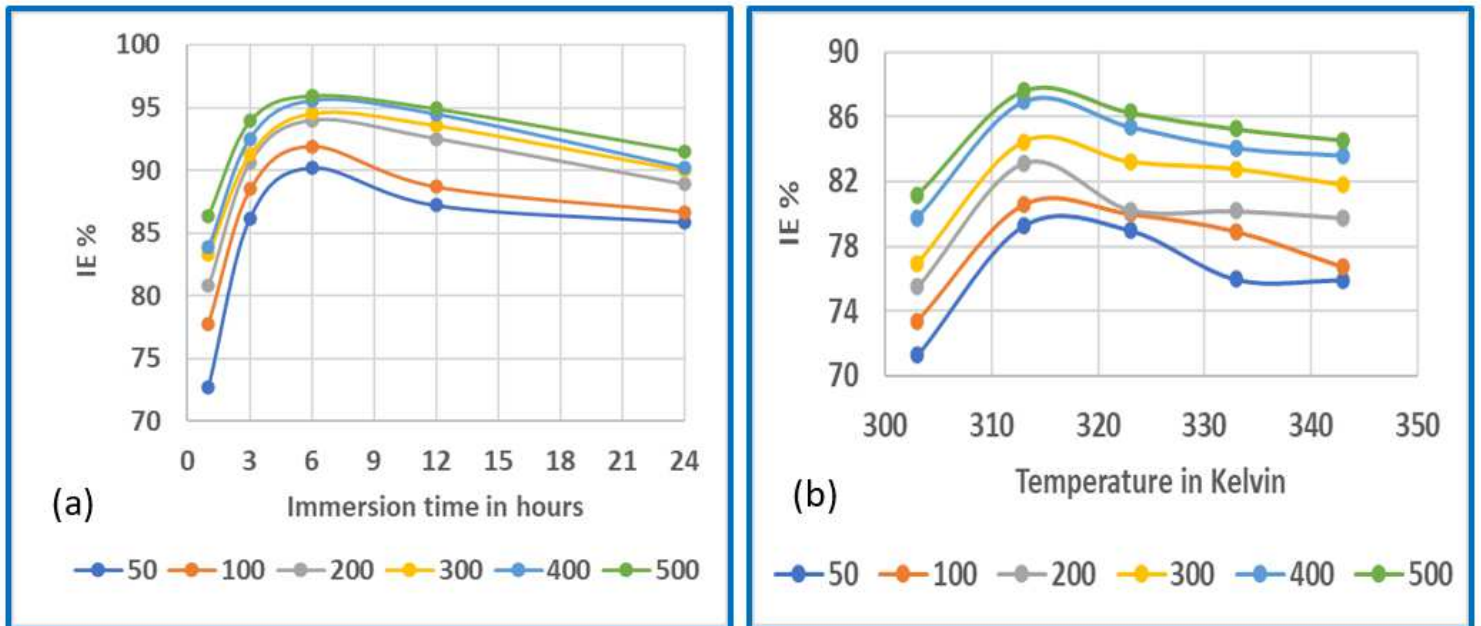


Figure 4

Change in corrosion inhibition performance of FCS for mild steel in 1 M HCl at various (a) immersion periods (b) temperatures

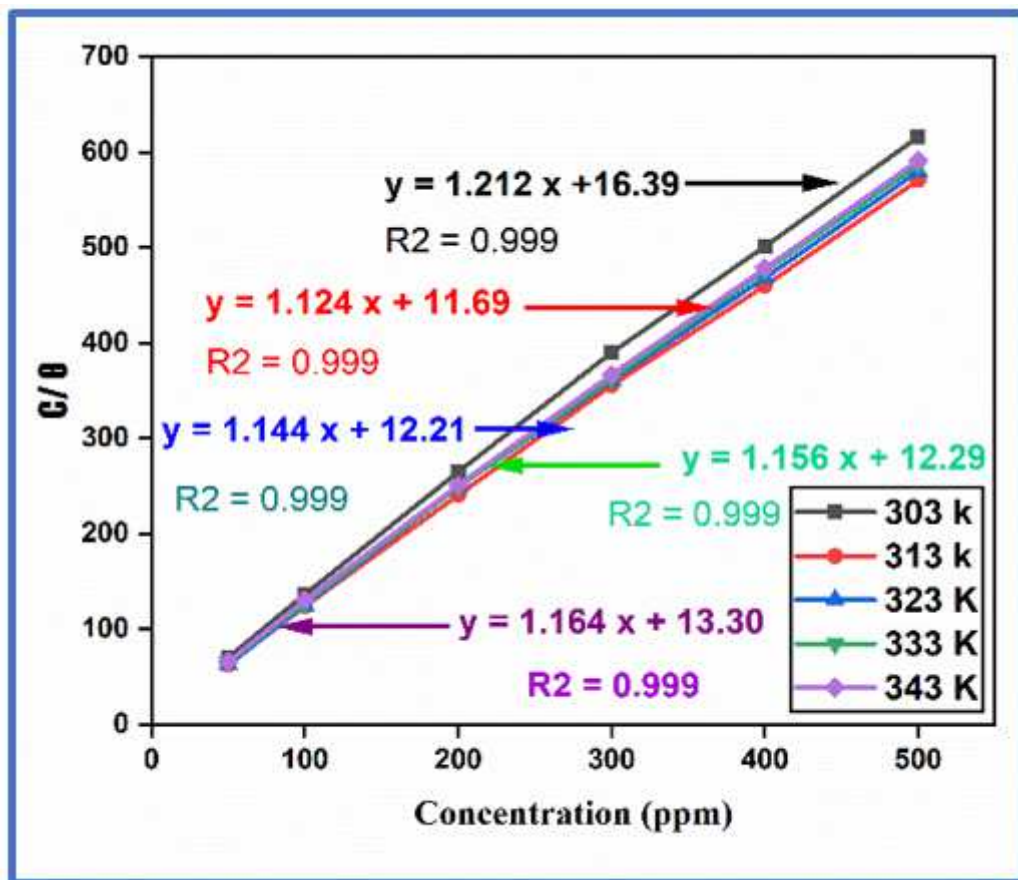


Figure 5

Langmuir isotherm plot for mild steel in 1 M HCl without and with FCS

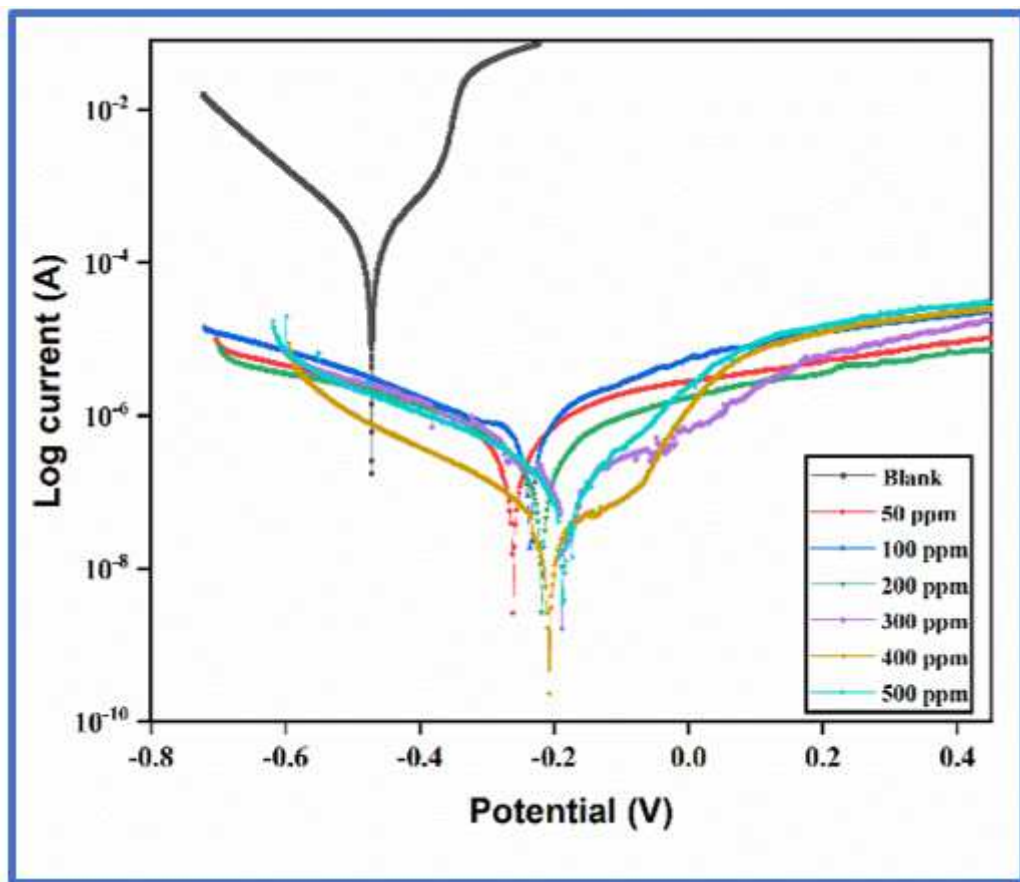


Figure 6

Tafel plot for mild steel in 1 M HCl with and without FCS

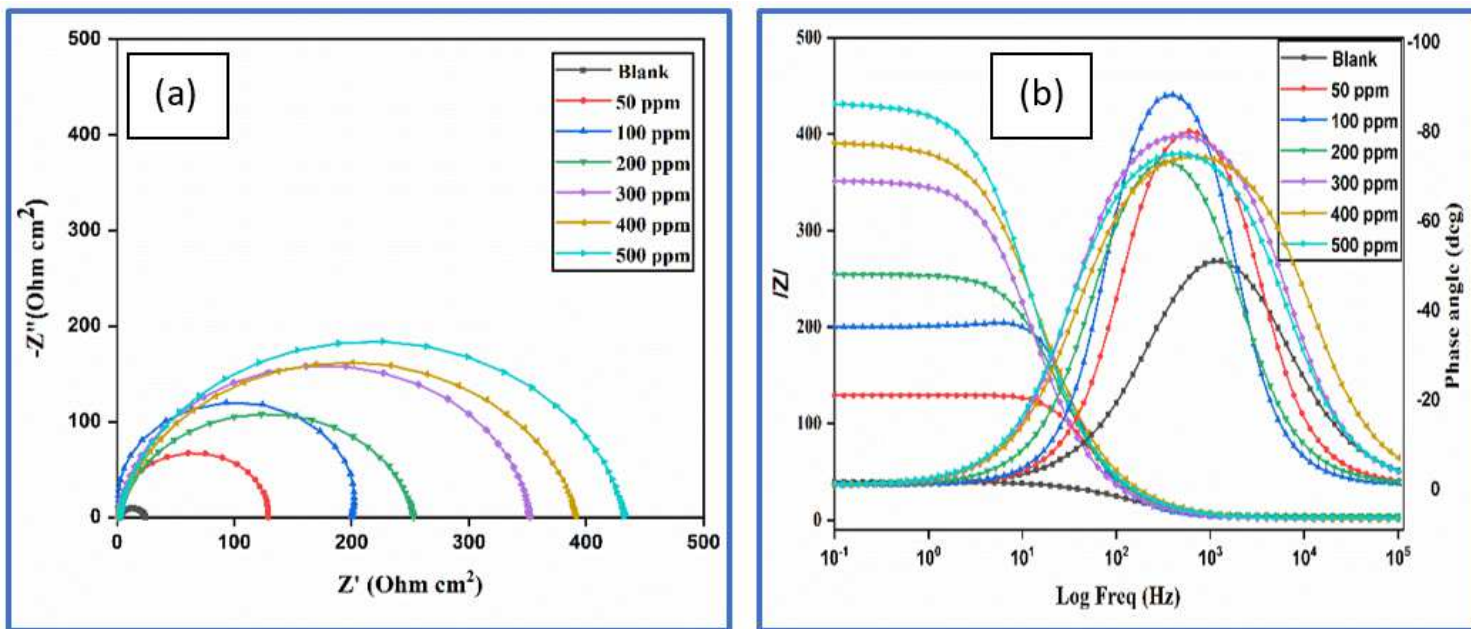


Figure 7

(a) Nyquist plot (b) Bodes , phase angle plots for mild steel in 1 M HCl without and with FCS inhibitor at 303 K

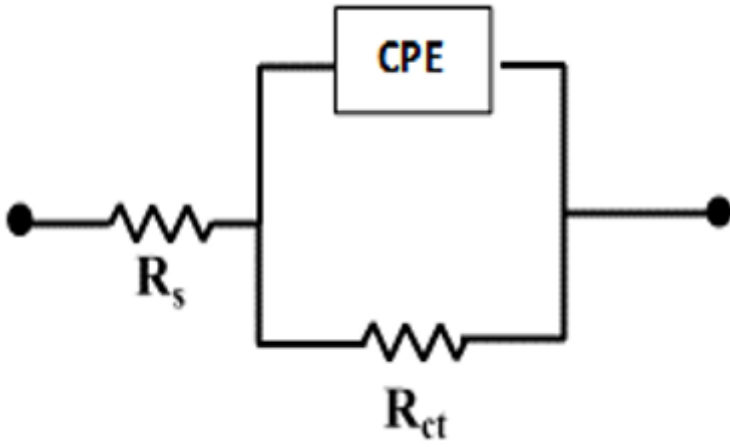


Figure 8

Equivalent circuit

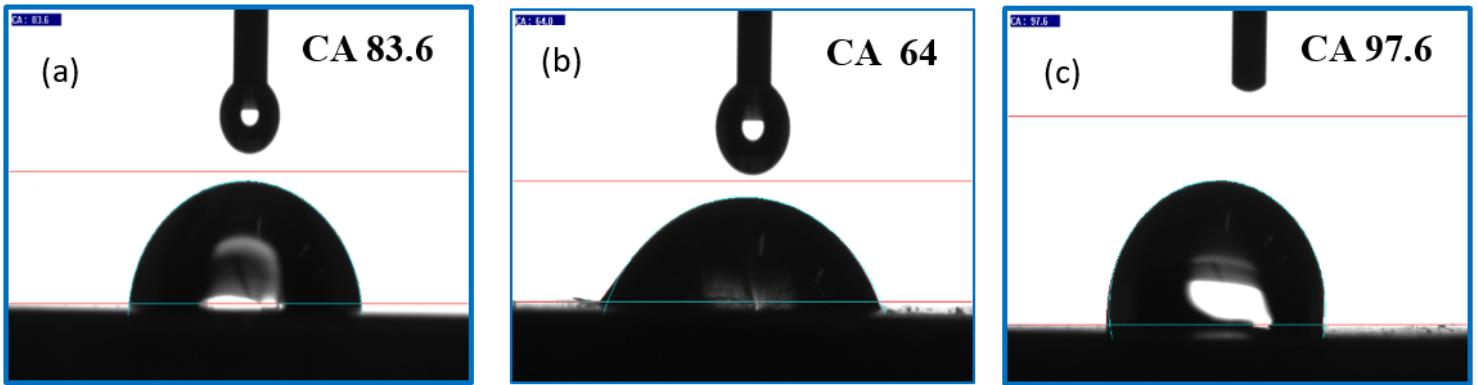


Figure 9

Contact angle of mild steel surfaces (a) plain (b) exposed to acid (c) exposed to acid containing the FCS inhibitor

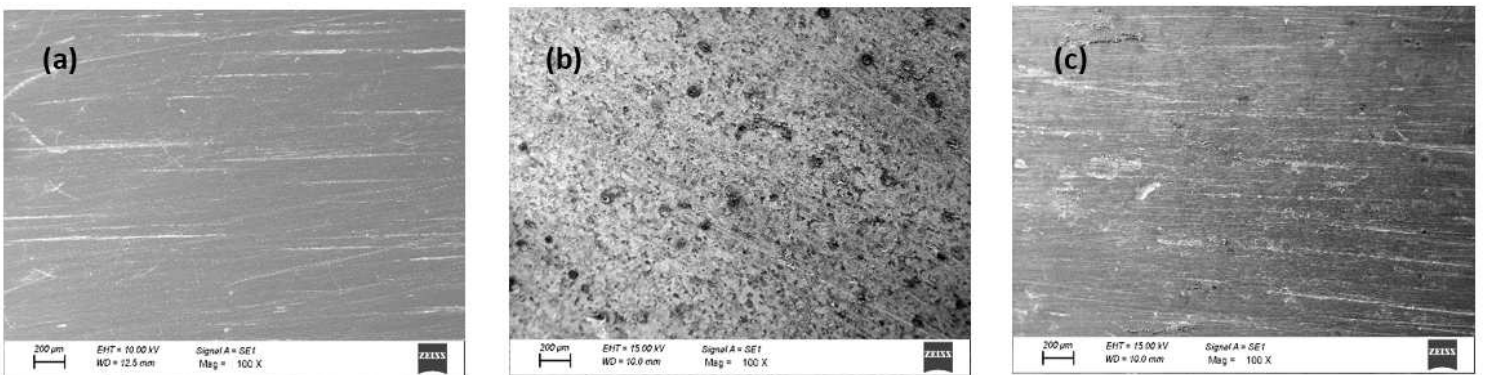


Figure 10

SEM image of the mild steel surfaces (a) plain (b) exposed to acid (c) exposed to acid containing FCS

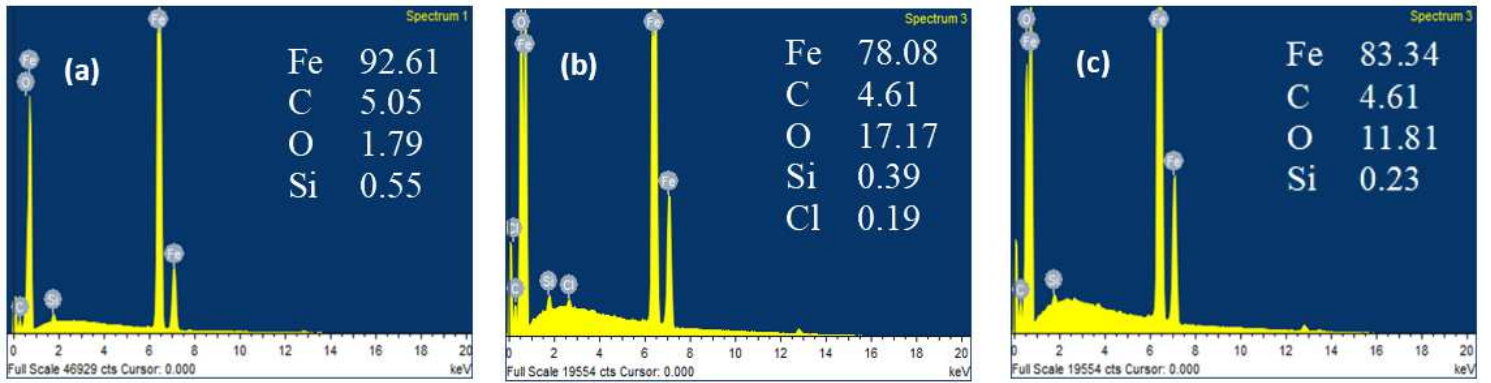


Figure 11

EDAX image of surfaces (a) plain metal (b) exposed to 1 M HCl (c) exposed to 1 M HCl containing FCS

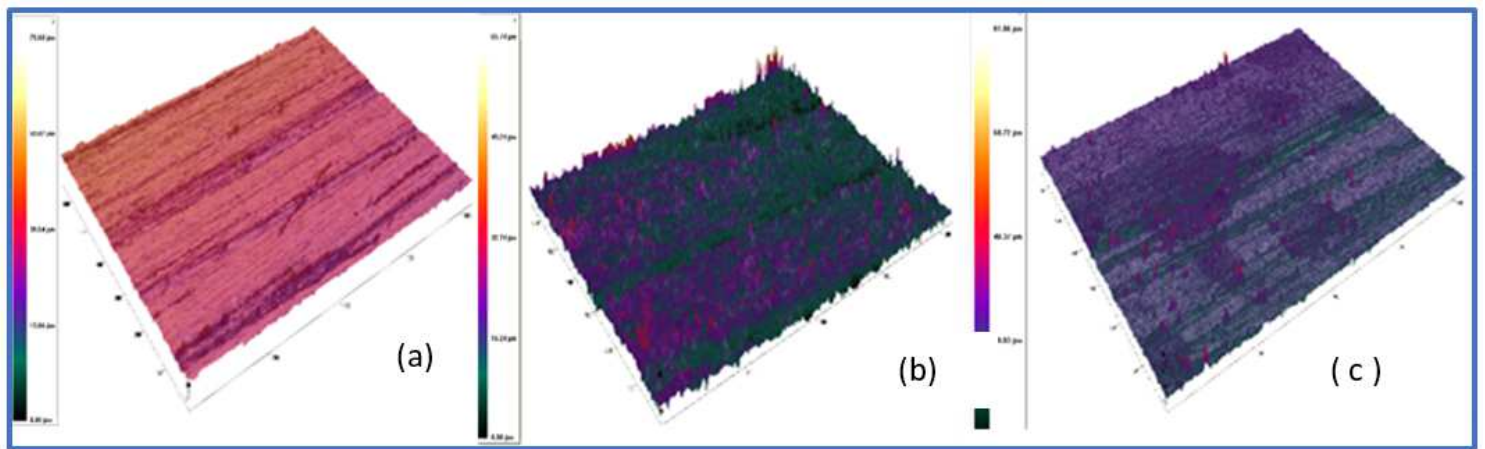


Figure 12

3D images of mild steel surfaces (a) Plain metal (b) exposed to acid and (c) exposed to acid containing FCS

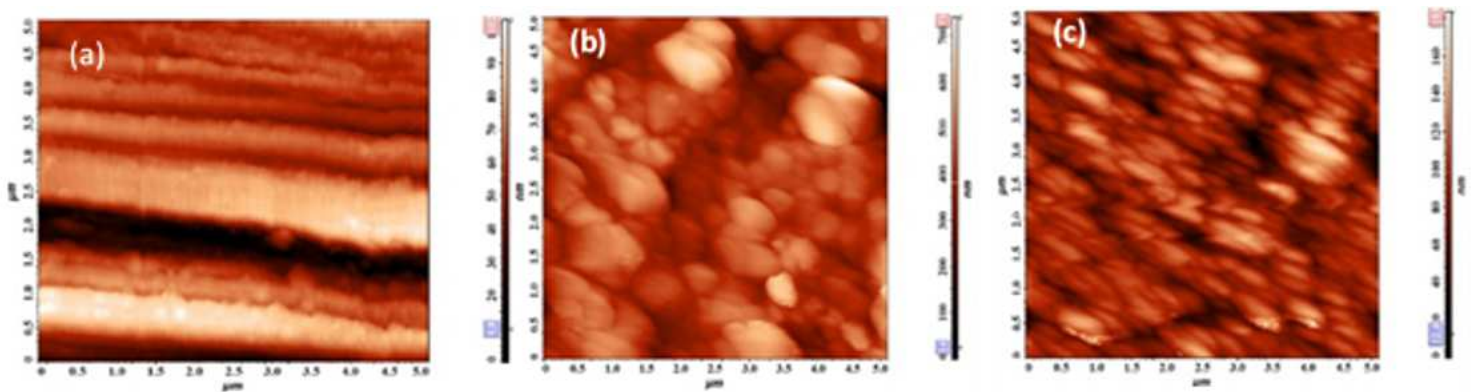


Figure 13

AFM (2D) image of surfaces (a) plain metal (b) exposed to 1 M HCl and (c) exposed to 1 M HCl containing FCS

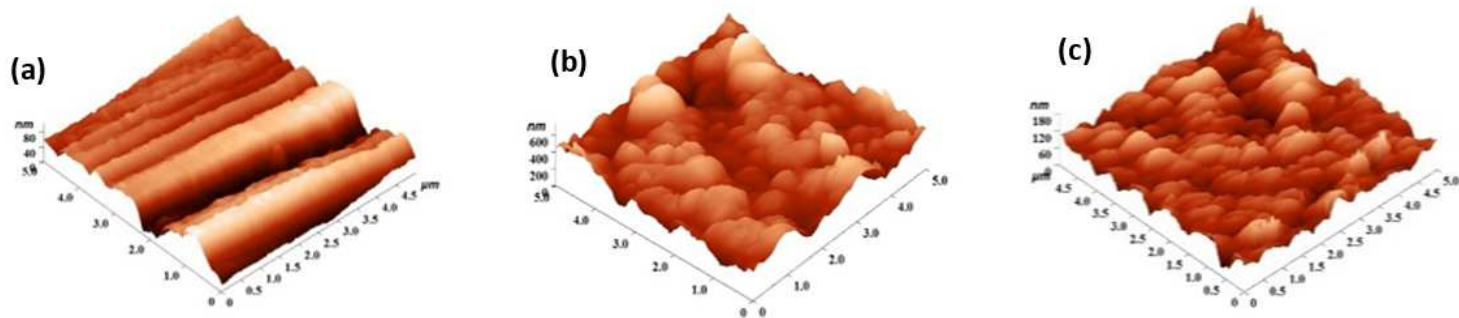


Figure 14

AFM (3 D) images of surfaces (a) plain metal (b) exposed to 1 M HCl and (c) exposed to 1 M HCl containing FCS

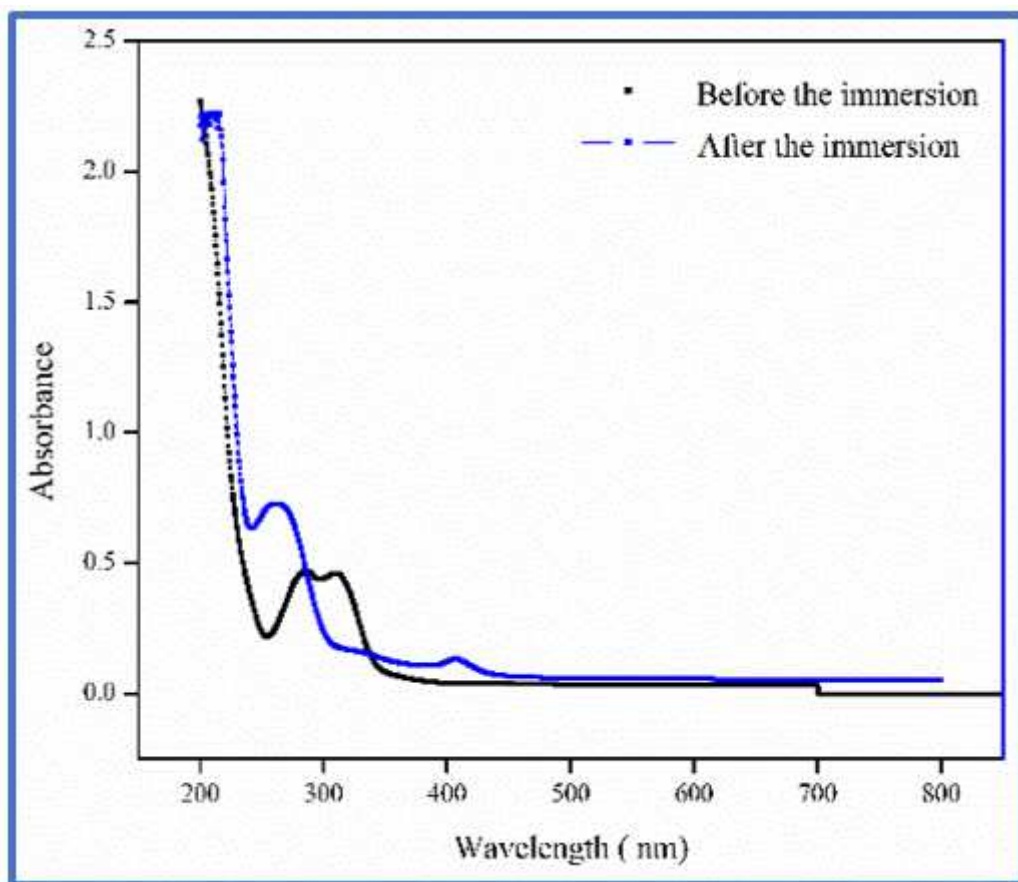


Figure 15

UV-visible spectra of FCS solution before and after introducing the mild steel samples

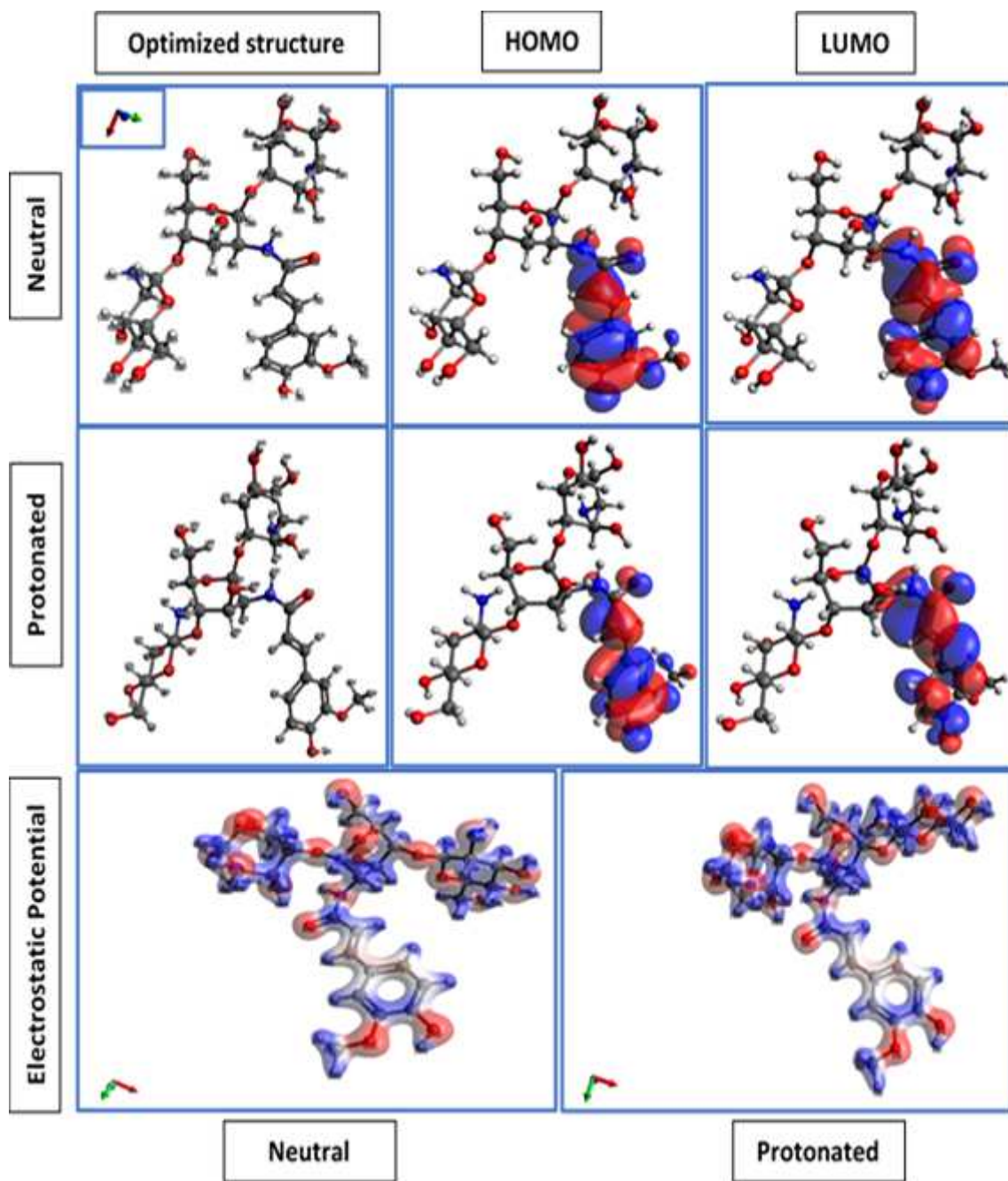
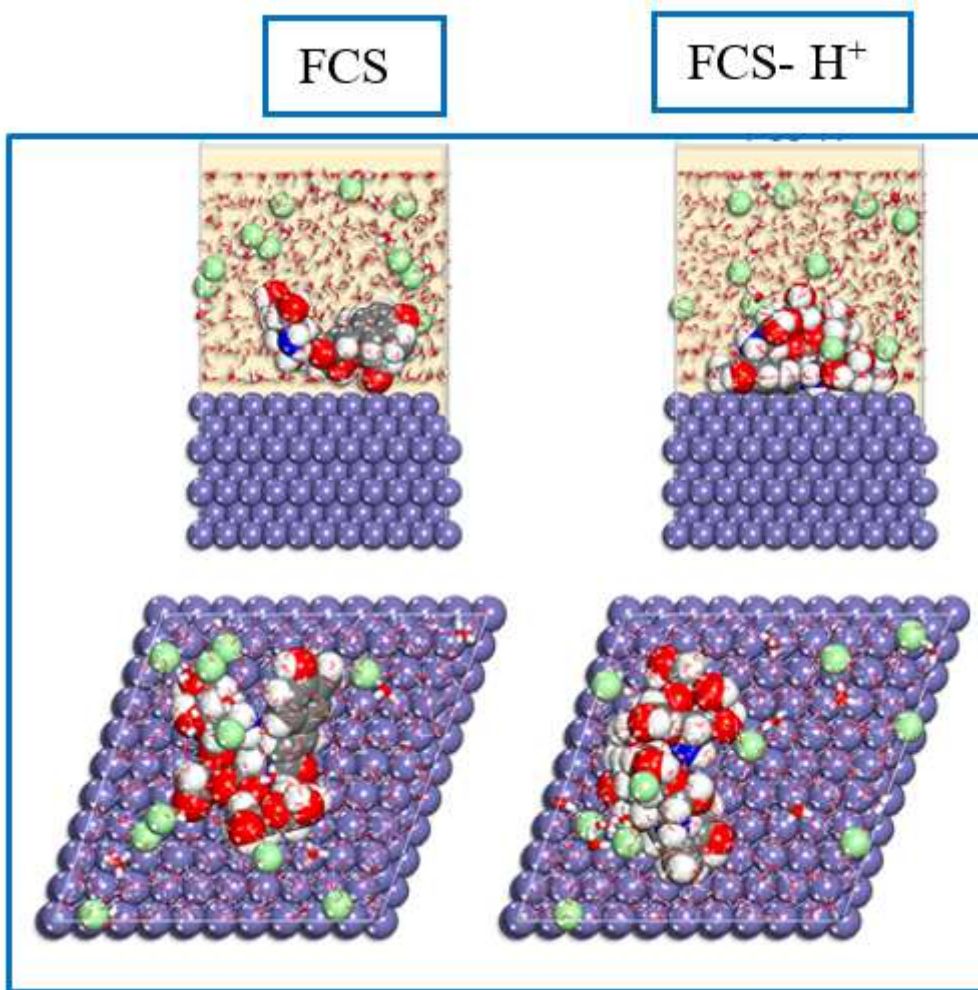


Figure 16

UV-visible spectra of FCS solution before and after introducing the mild steel samples



**Figure 17**

MC poses the lowest adsorption configurations for the FCS and FCS-H<sup>+</sup> in the simulated corrosion media on the Fe (1 1 0) surface

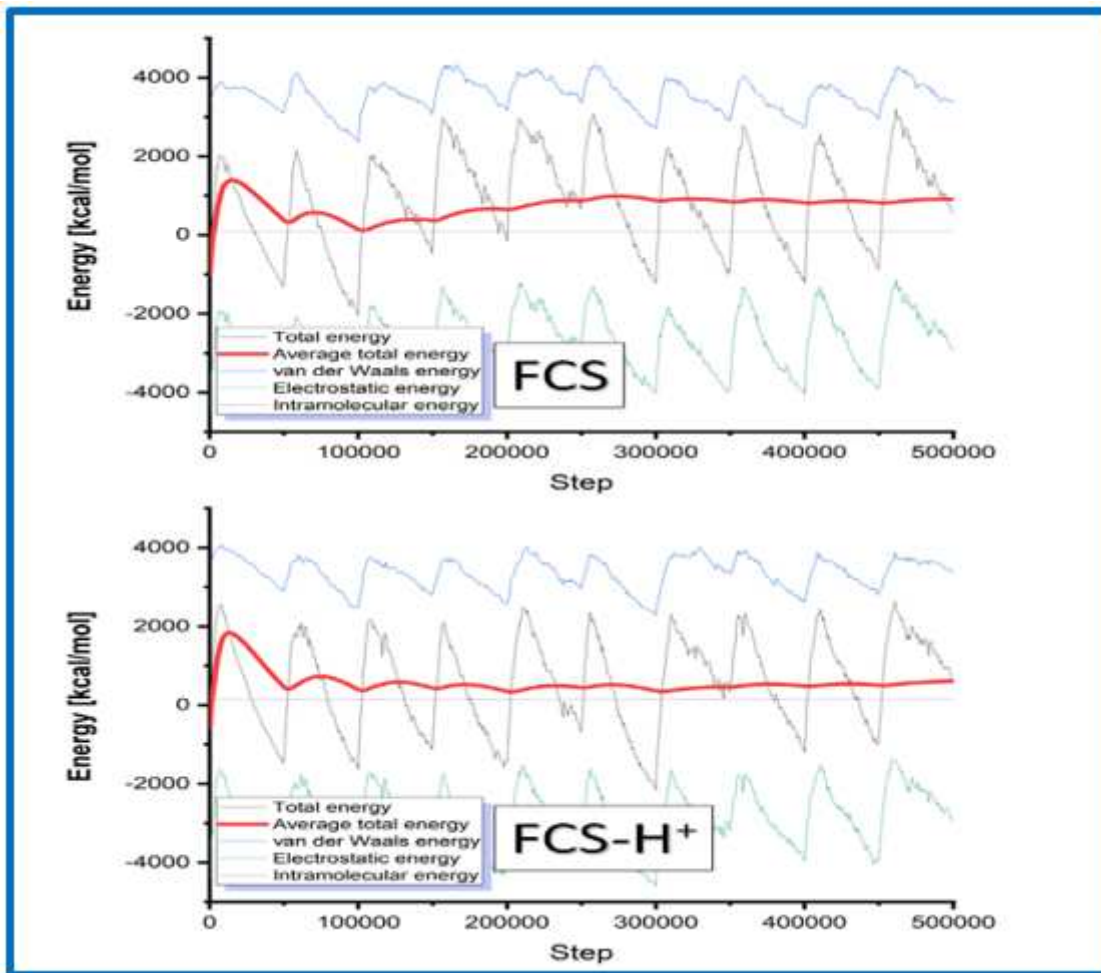


Figure 18

The presentation of the different energy terms contributions during the Monte Carlo calculations for FCS (neutral) and FCS-H<sup>+</sup> (protonated) inhibitor molecule

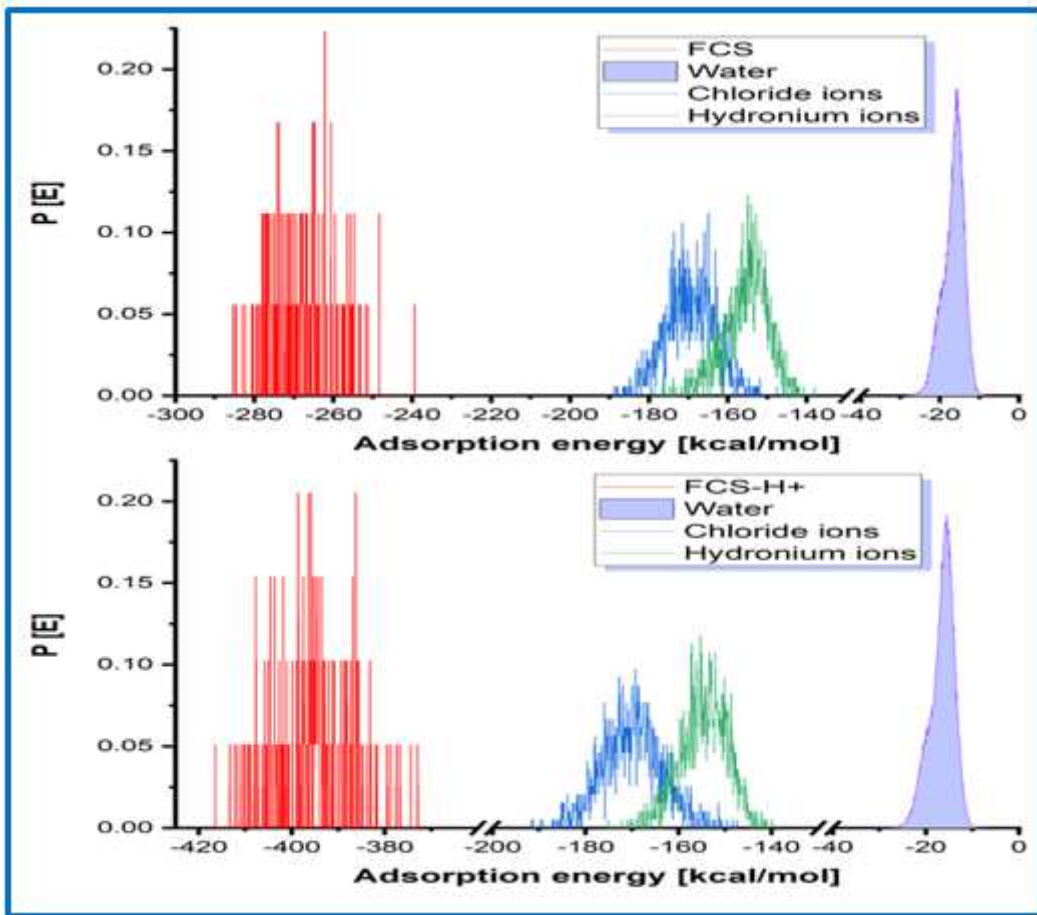
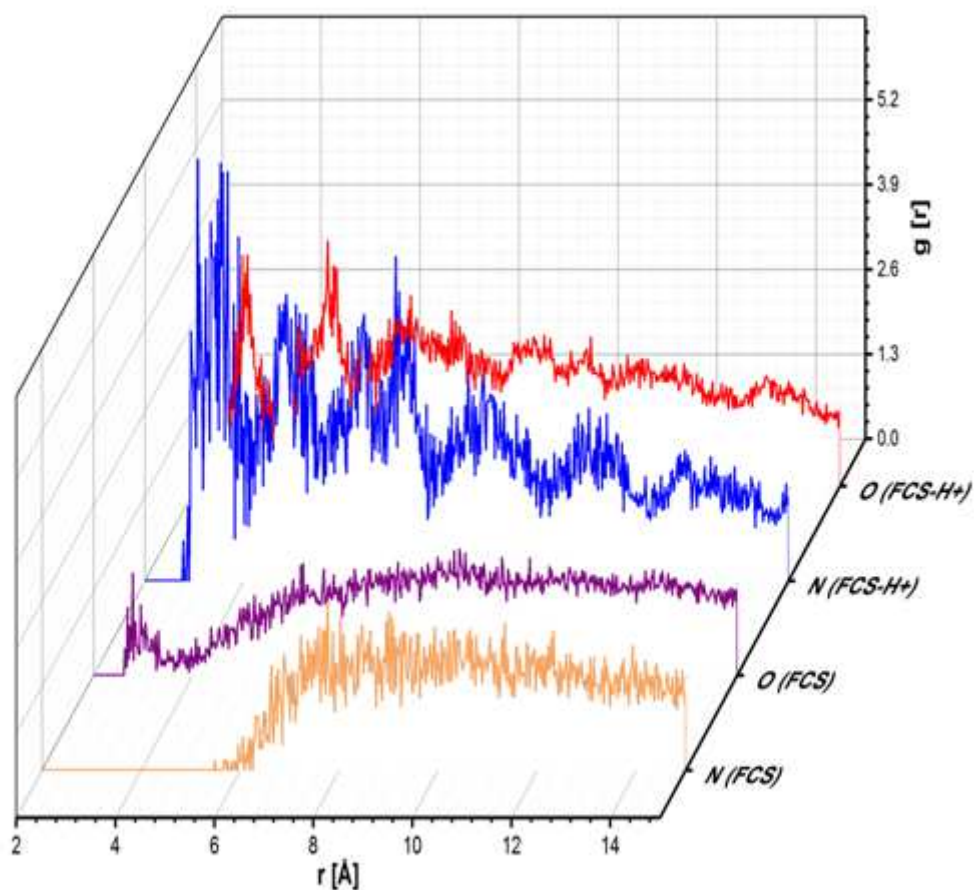


Figure 19

Distribution of adsorption energies for: FCS (neutral) and FCS-H<sup>+</sup> (protonated) inhibitor onto the Fe(110) surface



**Figure 21**

RDF of heteroatoms (nitrogen and oxygen,) for FCS and FCS-H<sup>+</sup> on the Fe surface obtained from MD trajectory

## Supplementary Files

This is a list of supplementary files associated with this preprint. Click to download.

- [GA.png](#)
- [Supplementaryinformation.docx](#)